

REPORT DOCUMENTATION PAGE

AFRL-SR-AR-TR-03-

Public reporting burden for the collection of information is estimated to average 1 hour per response, including gathering and maintaining the data needed, and completing and reviewing the collection of information. Send collection of information, including suggestions for reducing this burden, to Washington Headquarters Service, Davis Highway, Suite 1284, Arlington, VA 22202-4302, and to the Office of Management and Budget, Paperwork

0267

is on

1. AGENCY USE ONLY (Leave blank)		2. REPORT DATE 2/27/02		3. REPORT TYPE AND DATES COVERED Final - 5/1/96 - 10/31/01	
4. TITLE AND SUBTITLE Soft X-Ray Microscopy and Metrology				5. FUNDING NUMBERS FDF49620-96-1-0153	
6. AUTHOR(S) Professor David Attwood					
7. PERFORMING ORGANIZATION NAME(S) AND ADDRESS(ES) University of California, Berkeley Electronics Research Laboratory 253 Cory Hall Berkeley, CA 94705				8. PERFORMING ORGANIZATION REPORT NUMBER	
9. SPONSORING / MONITORING AGENCY NAME(S) AND ADDRESS(ES) AFOSR 801 North Randolph Street Arlington, VA 22203				10. SPONSORING / MONITORING AGENCY	
11. SUPPLEMENTARY NOTES					
12a. DISTRIBUTION / AVAILABILITY STATEMENT Unlimited DISTRIBUTION STATEMENT A Approved for Public Release Distribution Unlimited					
13. ABSTRACT (Maximum 200 words) The AFOSR grant has been used to support graduate students in the areas of coherence and microscopy at soft x-ray wavelengths. Techniques have been developed for characterizing the spatial coherence of undulator radiation, table top soft x-ray lasers, and high harmonic generation (HHG) of femtosecond pulses at short wavelengths, all in the 1-50 nm wavelength regime. With varying additional attributes, all three sources provide radiation exhibiting a high degree of spatial coherence. In the area of high resolution soft x-ray microscopy, a spatial resolution of 23nm has been demonstrated using new, best-in-the-world, Fresnel zone plate lenses, special nanometer test patterns, and bending magnet radiation in the 1-4nm region.					
14. SUBJECT TERMS soft x-ray wavelengths, coherence				15. NUMBER OF PAGES	
				16. PRICE CODE	
17. SECURITY CLASSIFICATION OF REPORT unclassified	18. SECURITY CLASSIFICATION OF THIS PAGE unclassified	19. SECURITY CLASSIFICATION OF ABSTRACT unclassified	20. LIMITATION OF ABSTRACT none		

BEST AVAILABLE COPY

20030731 055

Executive Summary For Final Report
AFOSR Grant FDF49620-96-1-0153
Soft X-Ray Microscopy and Metrology
Period of Performance: 5/1/96 – 10/31/01
Professor David Attwood, P.I.

EXECUTIVE SUMMARY

The AFOSR grant has been used to support graduate student research in the areas of coherence and microscopy at soft x-ray wavelengths. Techniques have been developed for characterizing the spatial coherence of undulator radiation, table top soft x-ray lasers and high harmonic generation (HHG) of femtosecond pulses at short wavelengths, all in the 1-50 nm wavelength regime. With varying additional attributes, all three sources provide radiation exhibiting a high degree of spatial coherence, an achievement that would have seemed very ambitious at the beginning of this contract. In the area of high resolution, soft x-ray microscopy, a spatial resolution of 23nm has been demonstrated using new, best-in-the-world, Fresnel zone plate lenses, special nanometer test patterns, and bending magnet radiation in the 1-4nm region. State-of-the-art images have been obtained of magnetic recording materials with sub-50nm domains, cryo-prepared biological samples showing detail views of cells and sub-cellular structures, modern nanochip interconnects, and more. Several students have received MS and PhD's working on these projects; six continue to do so today. A new text, based in large part on the AFOSR research support over the past 15 years, has been published: D. Attwood, Soft X-rays and Extreme Ultraviolet Radiation: Principles and Applications (Cambridge University Press, UK 2000). Lectures at UC Berkeley, based in large part on this same research, are now broadcast live free streaming over the internet (<http://webcast.berkeley.edu>), with participants across the U.S. and worldwide. The AFOSR grant has been a great enabler of science and technology, student training, and new industrial applications. Reprints of several recent reprints are attached.

DISTRIBUTION STATEMENT A
Approved for Public Release
Distribution Unlimited

BEST AVAILABLE COPY



ELSEVIER

Nuclear Instruments and Methods in Physics Research A 467-468 (2001) 841-844

**NUCLEAR
INSTRUMENTS
& METHODS
IN PHYSICS
RESEARCH**

Section A

www.elsevier.com/locate/nima

Soft X-ray microscopy to 25 nm with applications to biology and magnetic materials

G. Denbeaux^{a,*}, E. Anderson^a, W. Chao^{a,b}, T. Eimüller^c, L. Johnson^a,
M. Köhler^c, C. Larabell^d, M. Legros^a, P. Fischer^c, A. Pearson^a, G. Schütz^c,
D. Yager^d, D. Attwood^{a,b}

^aCenter for X-Ray Optics, Lawrence Berkeley National Laboratory, Berkeley, CA 94720, USA

^bElectrical Engineering and Computer Sciences Department, University of California, Berkeley, CA 94720, USA

^cExperimental Physics IV, University of Würzburg, D97074 Würzburg, Germany

^dLife Sciences Division, Lawrence Berkeley National Laboratory, Berkeley, CA 94720, USA

Abstract

We report both technical advances in soft X-ray microscopy (XRM) and applications furthered by these advances. With new zone plate lenses we record test pattern features with good modulation to 25 nm and smaller. In combination with fast cryofixation, sub-cellular images show very fine detail previously seen only in electron microscopy, but seen here in thick, hydrated, and unstained samples. The magnetic domain structure is studied at high spatial resolution with X-ray magnetic circular dichroism (X-MCD) as a huge element-specific magnetic contrast mechanism, occurring e.g. at the $L_{2,3}$ edges of transition metals. It can be used to distinguish between in-plane and out-of-plane contributions by tilting the sample. As XRM is a photon based technique, the magnetic images can be obtained in unlimited varying external magnetic fields. The images discussed have been obtained at the XM-1 soft X-ray microscope on beamline 6.1 at the Advanced Light Source in Berkeley. © 2001 Elsevier Science B.V. All rights reserved.

Keywords: X-ray microscopy; Cryogenic preservation; High resolution; Magnetic imaging

1. Introduction

The XM-1 X-ray microscope is located at the Advanced Light Source and provides high spatial resolution imaging of thick ($<10\mu\text{m}$) samples. The design allows a high throughput of a variety of samples in a wide variety of applications including biology, environmental science and materials science [1-3].

The illumination is provided by bending magnet radiation from the Advanced Light Source which is projected onto the sample through a condenser zone plate lens. The present condenser zone plate has a diameter of 9 mm, an outer zone width of 55 nm, and 41,000 zones. The illumination energy can be changed by the linear monochromator, which is composed of the condenser zone plate and a pinhole (approximately $10\mu\text{m}$ aperture) near the sample plane (typically $100\mu\text{m}$ from the sample plane). Due to the chromatic aberrations of zone plates, simply shifting the distance between the

*Corresponding author. Fax: +1-510-486-4550.

E-mail address: gdenbeaux@lbl.gov (G. Denbeaux).

condenser and the pinhole/sample plane shifts the illumination energy, which can be changed between 250 and 900 eV, and has been measured to have a spectral resolution of $E/\Delta E = 700$ [4].

The radiation passing through the sample is projected through the micro zone plate onto a CCD camera. The present micro zone plate has an outer zone width of 25 nm and a diameter of 63 μm . Both the micro zone plate and the condenser zone plate were fabricated by electron beam lithography by Erik Anderson at the Nanofabrication Laboratory in the Center for X-ray Optics [5]. The CCD camera is a 1024×1024 pixel array which is back-thinned and back-illuminated. It has a quantum efficiency of approximately 60–70% in the range of energies that the microscope operates.

Sample positions and focus can be pre-selected in a custom Zeiss Axioplan visible light microscope which is mutually indexed with the sample stage of XM-1. X-Y position accuracy is typically 2 μm over a 3 mm field with focal accuracy of 1 μm . This helps to allow the high throughput of samples. During a typical day, hundreds of images are collected.

The field of view of the microscope is 10 μm . In order to image larger samples, there is an automated montage assembly process which builds a larger image based on a series of sub-fields [6]. Using cross-correlation techniques, the smaller images are placed at the proper locations creating a nearly seamless montage.

2. Spatial resolution

In order to test the spatial resolution of the microscope, we used test patterns of grating patterns of various linewidths and duty cycles. They were fabricated with the same electron beam lithography tool that is used for the zone plates. An image of one test pattern is shown in Fig. 1(a). This test pattern has lines (light regions) with a width of 15 nm, separated by 45 nm spaces. The intensity across the lines is shown in Fig. 1(b). This shows a contrast of approximately 43%. This pattern of lines and spaces with a half-period of 30 nm can clearly be resolved. Another pattern

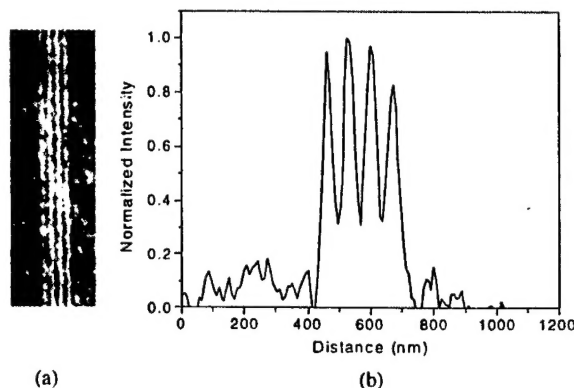


Fig. 1. (a) Image of test pattern with 15 nm lines (light) and 45 nm spaces (dark). The lines and spaces can clearly be resolved. (b) Intensity across the pattern averaged over adjacent line scans. This shows a contrast across the test pattern of approximately 43%.

with a half-period of 25 nm could also clearly be resolved and had a contrast of approximately 24%. We have not yet had a pattern with a half-period smaller than 25 nm, but if we project the modulation to smaller patterns, we expect to cross the Rayleigh Resolution Criterion of 15.3% contrast with a half-period pattern of 23 nm [7].

3. Magnetic materials

X-ray magnetic circular dichroism (X-MCD), i.e. the dependence of the absorption of circularly polarized X-rays onto the projection of the magnetization in a ferromagnetic absorber, yields magnetic contributions to the absorption cross-section as high as 25% for element-specific core level absorption edges, as e.g. the $L_{2,3}$ edges of transition metals. It has been shown recently that in combination with microscopies like photoemission electron microscopy [8] or soft X-ray microscopy [9], this can serve as a huge contrast mechanism to image the magnetic domain structure with high lateral resolution. Working in transmission, the magnetic absorption is conveniently measured by recording the transmitted photon intensities. Elliptically polarized light is obtained at the XM-1 from off-axis bend magnet radiation. A typical example is shown in Fig. 2

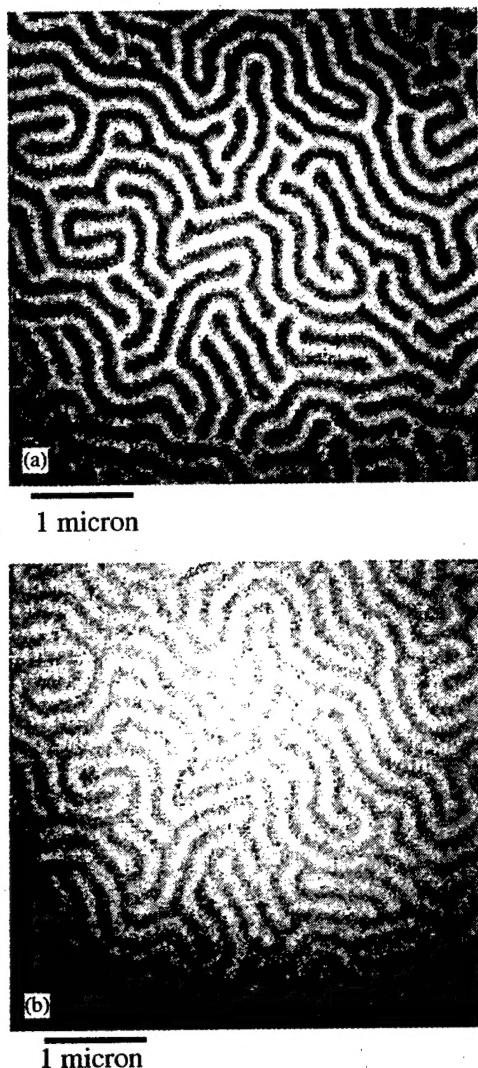


Fig. 2. Images of magnetization within an iron gadolinium multilayer, imaged at the iron L_{III} (a) and L_{II} (b) edges (707.5 and 720.5 eV, respectively). The expected contrast reversal of X-MCD between the edges can be seen.

where the self-organized magnetic domain pattern is shown. It has been obtained in a (0.4 nm Fe/0.4 nm Gd) \times 75 multilayer system with a pronounced out-of-plane anisotropy. To account for the limited penetration of soft X-rays, it has been prepared on a 35 nm Si_3N_4 membrane. The dark/light regions correspond to the Fe magnetization with its direction pointing in/out of the paper plane. As expected from the different spin-orbit

coupling, the magnetic contrast has a reversal between the L_3 and the L_2 edges which is a direct proof of the magnetic character of the pattern observed.

This is a photon based magnetic microscopy; thus, in principle, the domain structure can be recorded in unlimited external magnetic fields, which is of outstanding importance e.g. to proof the functionality of current devices, like magnetic sensors, MRAM, etc. The XM-1 is currently limited to apply magnetic fields up to ± 1000 Oe fields; however, this will be extended by a factor of three in the near future.

Since it is the projection of the local magnetization onto the photon propagation direction providing the contrast, in-plane magnetization, which is the most favorable configuration for magnetic systems of low dimensionality can be addressed by tilting the sample relative to the photon propagation direction. The first results have been recently obtained at the XM-1 [10]. Furthermore, the M-TXM allows to distinguish between in-plane and out-of-plane contributions to the magnetic domain structure. Together with the high sensitivity down to a few nanometers thickness due to the large magnetic contrast, this technique allows the study of magnetic microstructures and the reaction to external fields in current technologically relevant magnetic systems, like magnetic sensors (GMR, TMR), nanostructures, patterned media (MRAM) and high density storage media (magneto-optics).

4. Cryogenic sample preservation

In order to preserve the structural integrity of biological samples, a cryogenic sample holder has been built. The radiation dose for a typical exposure is approximately 10^7 Gy, which in some circumstances is enough to change the morphology of hydrated, room temperature biological samples [11,12]. The samples are frozen at a rate of about 3000°C/s to a temperature of about -130°C where they are maintained. The quick rate of freezing and the low final temperature are necessary to prevent the formation of ice crystals on a scale large enough to damage the sample.

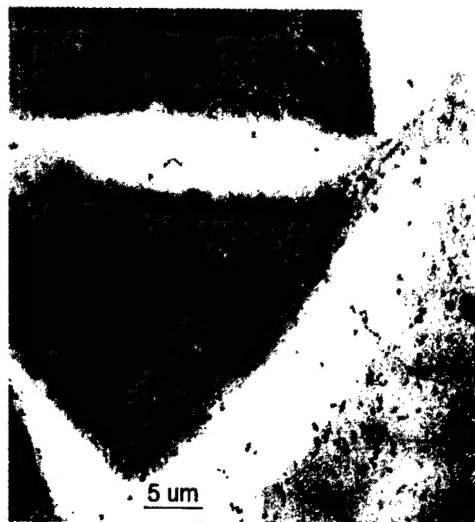


Fig. 3. Image of cryogenically preserved 3T3 fibroblast cells.

The freezing is accomplished by blowing helium gas, cooled to liquid nitrogen temperature, across the sample. Once the sample is properly frozen, it is able to withstand many exposures without any apparent changes in the morphology. During one test, the edge of the nuclear membrane of a fibroblast cell was imaged 40 times with no noticeable changes due to the accumulated radiation dose. Fig. 3 shows a cryogenically preserved 3T3 fibroblast cell. The cryogenic preservation allows imaging of the cell with remarkable detail.

5. Conclusion

Recent qualitative improvements including improved spatial resolution, cryogenic sample preservation, and the ability to image magnetic domains within samples provide new opportunities for X-ray microscopy as an important scientific tool. In particular, soft X-ray microscopy in combination with X-MCD for imaging of magnetic microstructure is a powerful tool for technologically relevant current nanopatterned

magnetic media. With these capabilities, the XM-1 is in use for high resolution imaging of a wide variety of scientific studies including biology and magnetic materials.

References

- [1] W. Meyer-Ilse, G. Denbeaux, L.E. Johnson, W. Bates, A. Lucero, E. Anderson, The high resolution X-ray microscope, XM-1, in: W. Meyer-Ilse, T. Warwick, D. Attwood (Eds.), *X-Ray Microscopy*, Vol. 507, American Institute of Physics, Melville, 2000, pp. 129–134.
- [2] W. Meyer-Ilse, H. Medeck, L. Jochum, E.H. Anderson, D. Attwood, C. Magowan, R. Balhorn, M. Moronne, D. Rudolph, G. Schmahl, *Synchrotron Radiat. News* 8 (1995) 23–33.
- [3] P. Fischer, T. Eimüller, G. Schütz, G. Bayreuther, S. Tsunashima, N. Takagi, G. Denbeaux, D. Attwood, magnetic domains in nanostructured media studied with M-TXM, *J. Synchrotron Rad.* 8 (2001) 325.
- [4] G. Denbeaux, L.E. Johnson, W. Meyer-Ilse, Spectromicroscopy at the XM-1, in: W. Meyer-Ilse, T. Warwick, D. Attwood (Eds.), *X-Ray Microscopy*, Vol. 507, American Institute of Physics, Melville, 2000, pp. 478–483.
- [5] E.H. Anderson, D.L. Olynick, B. Harteneck, E. Veklerov, G. Denbeaux, W. Chao, A. Lucero, L. Johnson, D. Attwood Jr., *Nanofabrication and Diffractive Optics for High-Resolution X-ray Applications*, *J. Vac. Sci. Technol.* 18 (6) (2000) 2970.
- [6] B. W. Loo Jr., W. Meyer-Ilse, S.S. Rothman, *J. Microsc.* Part 2, 197 (2000) 185.
- [7] M. Born, E. Wolf, *Principles of Optics*, 6th Edition, Cambridge University Press, Cambridge, 1980.
- [8] J. Stohr, Y. Wu, B.D. Hermsmeier, M.G. Samant, G.R. Harp, S. Koranda, D. Dunham, B.P. Tonner, *Science* 259 (1993) 658.
- [9] P. Fischer, G. Schütz, G. Schmahl, P. Guttman, D. Raasch, *Z. Phys. B* 101 (1996) 313.
- [10] P. Fischer, T. Eimüller, G. Schütz, M. Köhler, G. Bayreuther, G. Denbeaux, D. Attwood, Study of in-plane magnetic domains with Magnetic Transmission X-ray Microscopy, *J. Appl. Phys.* (2001), submitted.
- [11] G. Schneider, *Ultramicroscopy* 75 (1998) 85.
- [12] J. Maser, C. Jacobsen, J. Kirz, A. Osanna, S. Spectro, S. Wang, J. Warnking, Development of a cryo scanning transmission X-ray microscope at the NSLS, in: J. Thieme, G. Schmahl, D. Rudolph, E. Umbach (Eds.), *X-ray Microscopy and Spectromicroscopy*, Springer, Berlin, 1992, pp. 1–35.



ELSEVIER

Nuclear Instruments and Methods in Physics Research A 467–468 (2001) 913–916

**NUCLEAR
INSTRUMENTS
& METHODS
IN PHYSICS
RESEARCH**
Section A

www.elsevier.com/locate/nima

Spatial coherence properties of undulator radiation based on Thompson–Wolf two-pinhole measurement

Chang Chang^{a,b,*}, Patrick Naulleau^a, Erik Anderson^a, David Attwood^{a,b}^a Center for X-Ray Optics, Lawrence Berkeley National Laboratory, One Cyclotron Rd., Mailstop 2-400, Berkeley, CA 94720, USA^b Department of Electrical Engineering & Computer Science, University of California, Berkeley, CA 94720, USA

Abstract

The Thompson–Wolf two-pinhole technique was used to characterize the spatial coherence properties of undulator radiation. Both vertical and horizontal coherence properties are measured with various pinhole separations. High spatial coherence of extreme ultraviolet undulator radiation is demonstrated. © 2001 Elsevier Science B.V. All rights reserved.

1. Introduction

While coherent radiation has been readily available and widely utilized at visible wavelengths for many years [1–3], it is just becoming available for wide use at shorter wavelengths due to the advent of undulator radiation at modern synchrotron facilities [4–7]. Recent progress with EUV lasers [8], high laser harmonics [9,10], and free electron lasers [11] may soon add to these capabilities. In the experiment reported here, the classic two-pinhole diffraction technique [1] is used to characterize the degree of spatial coherence provided by undulator radiation. The complete characterization of the spatial coherence properties of the undulator can be found in Ref. [12].

2. Experiment

A simplified schematic setup of this experiment is shown in Fig. 1. A more detailed experiment setup is shown in Ref. [12]. The beamline [13] provides an overall 60:1 demagnified image of the source in the exit plane of the beamline.¹ The undulator employed at this beam-line has a magnet period (λ_u) of 8 cm, 55 magnet periods (N), and a non-dimensional magnetic field parameter $K=2.7$, for operation at $\lambda=13.4$ nm. The electron beam energy is 1.9 GeV. The beam size at the undulator exit is approximately Gaussian with $(\sigma_x, \sigma_y)=(260 \mu\text{m}, 16 \mu\text{m})$ [13]. The acceptance half-angle (NA) of undulator radiation for these experiments is $48 \mu\text{rad}$, which is somewhat smaller than the central radiation cone 2 half-angle of $80 \mu\text{rad}$ for finite K [4,13]. The radiation within θ_{cen} has a natural bandwidth of $\lambda/\Delta\lambda=N$, corresponding to a longitudinal coherence length,

*Corresponding author. Tel.: +1-510-486-6106; fax: +1-510-486-4550.

E-mail addresses: cnchang@lbl.gov, chang2@eecs.berkeley.edu (C. Chang).

¹ The beamline actually consists of three focusing mirrors, a grating monochromator, and two limiting apertures. A detailed description of the beamline is in Ref. [13].

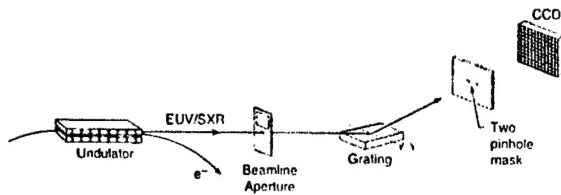


Fig. 1. A simplified schematic plot of the experimental setup showing only the essential elements of the beamline. The two pinholes are shown here with a horizontal separation; vertical separation tests are also employed. A more complete description of the beamline is given in Ref. [13].

$l_{\text{coh}} = \lambda/2\Delta\lambda = 0.37 \mu\text{m}$. The monochromator bandpass of this beamline can be narrowed, providing a value of $\lambda/\Delta\lambda$ as high as 1100, by adjusting the size of its horizontal exit-slit. Except where stated otherwise, all experiments reported in this paper were performed with the monochromator exit-slit set such as to pass the entire $\lambda/\Delta\lambda = 55$

natural bandwidth associated with the central cone. Accounting for the $48\text{-}\mu\text{rad}$ acceptance NA, the spatially coherent power is expected to be about 12 mW, within a relative bandwidth of $\lambda/\Delta\lambda = 55$ at $\lambda = 13.4 \text{ nm}$ [13]. This bandwidth is sufficient to assure that the quasi-monochromatic condition required for this experiment is satisfied, i.e. that the temporal coherence does not significantly affect fringe visibility.

To implement these coherence tests, a patterned mask containing multiple pairs of 450-nm -diameter-pinhole, with pinhole-pair separations ranging from 1 to $9 \mu\text{m}$, was placed in the vicinity of the beamline exit plane, i.e. at the demagnified image of the undulator source. The 450-nm pinhole diameter is chosen to be significantly smaller than the expected coherence width, while providing reasonable throughput and appropriate working distance for full Airy pattern recording at the charge-coupled-device (CCD) electronic array

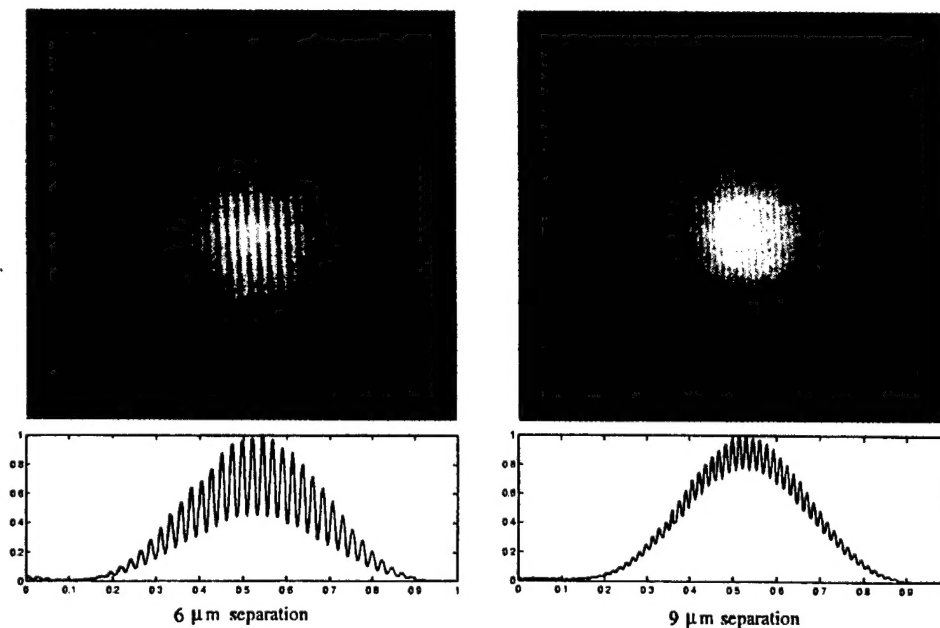


Fig. 2. Measured two-pinhole interference patterns for horizontal pinhole separations of 6 and $9 \mu\text{m}$, for a wavelength of 13.4 nm and a beamline acceptance half-angle of $48 \mu\text{rad}$. The pinhole diffraction patterns overlap and produce an interference pattern within the Airy envelope. The interference patterns are recorded on an EUV sensitive CCD camera, located 26 cm downstream of the pinhole mask. Pinhole diameters range from 400 to 500 nm , but are equal in their respective pairs. As shown in the lineouts, fringe visibility of the modulation decreases for larger separations (0.4 for $6 \mu\text{m}$ and 0.14 for $9 \mu\text{m}$), indicating reduced spatial coherence. Spectral resolution for these measurements is 55 .

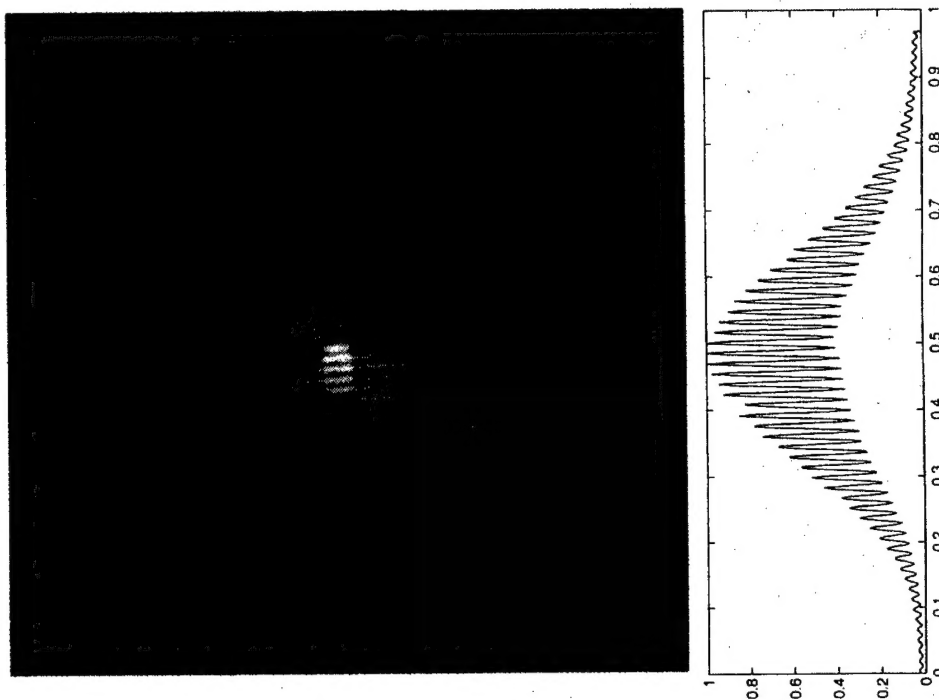


Fig. 3. Measured two-pinhole interference patterns for a vertical pinhole separation of $9\text{ }\mu\text{m}$, a wavelength of 13.4 nm , and an acceptance half-angle of $48\text{ }\mu\text{rad}$. Comparing with the horizontal $9\text{ }\mu\text{m}$ separation pattern in Fig. 2, the fringe visibility is seen to be 0.43 in the vertical case, indicating a higher degree of coherence.

detector. The mask, fabricated using electron-beam lithography and reactive-ion etching, consists of a 360-nm -thick Ni absorbing layer evaporated on a 100-nm -thick Si_3N_4 membrane. The mask features are etched completely through the membrane prior to the Ni evaporation, leaving the pinholes completely open in the finished mask. Pinhole circularity and size are confirmed by observing the resultant far field Airy patterns, as recorded on an the CCD.

The pinhole array mask is mounted on an x - y - z stage, allowing desired pinhole separations to be selected sequentially, and the coherence to be studied as a function of focal position. A back-thinned, back-illuminated, EUV sensitive CCD camera is placed 26 cm downstream of the mask to record the resulting interference pattern. The active area of the CCD is $25.4\text{ mm} \times 25.4\text{ mm}$, in a 1024×1024 pixel array. Typical exposure times for a recorded

pattern vary between 50 ms and 5 s depending on pinhole separation, storage ring current, and beamline apertures.

Fig. 2 shows the recorded interference patterns for horizontal pinhole separations of 6 and $9\text{ }\mu\text{m}$. The measured magnitude of the fringe visibility decreases with larger pinhole separation as expected. Fig. 3 shows an interference pattern obtained with vertically displaced pinhole pairs. Fringe modulation is generally better than that of horizontally displaced pinholes. In order to verify our ability to control and measure the beamline coherence properties, the measurement was repeated at a larger beamline acceptance NA. This NA can be controlled by way of the acceptance aperture described above. The measured spatial coherence decreases 60% in both directions as expected when the $48\text{ }\mu\text{rad}$ acceptance aperture is replaced by a larger aperture allowing the entire $80\text{ }\mu\text{rad}$ central radiation cone to pass. A more

complete set of data, at different separations, is shown in Ref. [12].

For a large incoherent source, the Van Cittert–Zernike theorem gives a spatial coherence profile of an Airy pattern, where

$$d_{\text{null}}\theta = 1.22\lambda, \quad (1)$$

d_{null} is the first null diameter of the coherence profile, θ is the image-side NA and λ is the wavelength. Given the beamline acceptance NA of 48 μrad , demagnification of 60:1 and wavelength of 13.4 nm, the first null diameter is 5.7 μm . Thus a spatial coherence scale of around 5–6 μm in the exit plane of the beamline is expected. This simple theory needs to be corrected for smaller source size, aberrations in the beamline optics, and specific beamline geometry. For example, account must be taken for the electron beam phase-space. In general for synchrotron radiation, we have a smaller phase-space in vertical plane than we do in horizontal plane. Thus we expect better coherence properties in the vertical plane, as observed in comparing Figs. 2 and 3.

3. Conclusion

We have measured the spatial coherence of spatially filtered undulator radiation. A very high degree of spatial coherence is demonstrated, as expected on the basis of a simple model. Based on these observations and well understood scaling of undulator radiation, high average power, spatially coherent radiation is confirmed at modern storage rings with the use of appropriate pinhole spatial filtering techniques. The extension of these results from EUV to soft X-ray and X-ray wavelength is expected to be straightforward.

Acknowledgements

The authors would like to thank Dr. Kenneth Goldberg for valuable discussion. Special thanks are due to the entire CXRO engineering team and most notably to Phil Batson, Paul Denham, Drew Kemp and Gideon Jones for bringing the experimental hardware to fruition. This work was supported in part by the Office of Basic Energy Sciences, Department of Energy, by DARPA's Advanced Lithography Program, by the Air Force Office of Scientific Research, by Intel Corporation, and by the Extreme Ultraviolet Lithography Limited Liability Corporation.

References

- [1] B.J. Thompson, E. Wolf, *J. Opt. Soc. Am.* 47 (1957) 895.
- [2] M. Born, E. Wolf, *Principles of Optics*, 7th Edition, Cambridge University Press, Cambridge UK, 1999.
- [3] J.W. Goodman, *Statistical Optics*, Wiley, New York, 1985.
- [4] D.T. Attwood, *Soft X-Rays and Extreme Ultraviolet Radiation*, Cambridge University Press, Cambridge UK, 1999 (Chapters 5 and 8).
- [5] D. Attwood et al., *Science* 228 (1985) 1265.
- [6] R. Coisson, *Appl. Optics* 34 (1995) 904.
- [7] Y. Takayama et al., *J. of Synchrotr. Radiat.* 5 (1998) 456.
- [8] M.C. Marconi et al., *Phys. Rev. Lett.* 79 (1997) 2799; Y. Liu et al., to be published.
- [9] C. Spielmann et al., *Science* 278 (1998) 661.
- [10] A. Rundquist et al., *Science* 280 (1998) 1412.
- [11] J. Andruszkow et al., First observation of self-amplified spontaneous emission in a free-electron laser at 109 nm wavelength. *Phys. Rev. Lett.* (2000), accepted for publication.
- [12] C. Chang et al., *Opt. Commun.* 182 (2000) 25.
- [13] D. Attwood et al., *IEEE J. Quantum Electron.* 35 (1999) 709.



ELSEVIER

1 August 2000

OPTICS
COMMUNICATIONS

Optics Communications 182 (2000) 25–34

www.elsevier.com/locate/optcom

Spatial coherence characterization of undulator radiation

Chang Chang^{a,b,*}, Patrick Naulleau^a, Erik Anderson^a, David Attwood^{a,b}^a Center for X-Ray Optics, Lawrence Berkeley National Laboratory, Berkeley, CA 94720, USA^b Department of Electrical Engineering & Computer Science, University of California, Berkeley, CA 94720, USA

Received 12 April 2000; accepted 8 June 2000

Abstract

The coherence properties of undulator radiation at extreme ultraviolet (EUV) wavelengths are measured using the Thompson–Wolf two-pinhole method. The effects of asymmetric source size and beamline apertures are observed. High spatial coherence EUV radiation is demonstrated. Projection of these same capabilities to the x-ray region is straightforward. Published by Elsevier Science B.V.

1. Introduction

Coherent radiation offers important opportunities for both science and technology. The well defined phase relationships characteristic of coherent radiation, allow for diffraction-limited focusing (as in scanning microscopy), set angular limits on diffraction (as in protein crystallography), and enable the convenient recording of interference patterns (as in interferometry and holography). While coherent radiation has been readily available and widely utilized at visible wavelengths for many years [1–5], it is just becoming available for wide use at shorter wavelengths [6]. This is of great interest as the shorter wavelengths, from the extreme ultraviolet (EUV, 10–20 nm wavelength), soft x-ray (1–10 nm), and x-ray (< 1 nm) regions of the spectrum, correspond to photon energies that are well matched to the primary electronic resonances (K-shell, L-shell, etc.)

of essentially all elements, thus providing a powerful combination of techniques for the elemental and chemical analysis of physical and biological materials at very high spatial resolution. Tunable, coherent radiation in these spectral regions is available primarily due to the advent of undulator radiation at modern synchrotron facilities [7–12], where relativistic electron beams of small cross-section transverse periodic magnet structures, radiating very bright, powerful, and spatially coherent radiation at short wavelengths. Recent progress with EUV lasers [13], high laser harmonics [14,15], and free electron lasers [16] may soon add to these capabilities. In this paper we utilize the classic two-pinhole diffraction technique [2], an extension of Young's two-slit interference experiment [1], to simply and accurately characterize the degree of spatial coherence provided by undulator radiation. We show that, with the aid of modest pinhole spatial filtering, undulator radiation can provide tunable short wavelength radiation with a very high degree of spatial coherence at presently available user facilities. Spatially coherent power of

* Corresponding author. Fax: +1-510-486-6103; e-mail: cnchang@lbl.gov

order 30 mW is available in the EUV [17], and is expected to scale linearly with wavelength to about 0.3 mW in the hard x-ray region [6].

For radiation with a high degree of coherence and a well-defined propagation direction, it is convenient to describe coherence properties in longitudinal and transverse directions. For a source of diameter d , emission half-angle θ , and full spectral bandwidth $\Delta\lambda$ at wavelength λ , relationships for full spatial coherence and longitudinal coherence length, l_{coh} , are given respectively by

$$d \cdot \theta = \lambda/2\pi \quad (1)$$

and

$$l_{\text{coh}} = \lambda^2/2\Delta\lambda, \quad (2)$$

where d , θ , and $\Delta\lambda$ are $1/\sqrt{e}$ measures of Gaussian distributions. Based on measures of the source size and theoretical predictions of the emission angle, it is estimated that undulator radiation, as discussed in this paper, emanating from an electron beam of highly elliptical cross-section, will approach full spatial coherence Eq. (1) in the vertical plane, while being coherent over only a fraction of the radiated beam in the horizontal direction. Here we present a detailed characterization of an undulator beamline optimized for operation in the EUV regime [17].

Undulator beamline 12.0 at Lawrence Berkeley National Laboratory's Advanced Light Source (ALS) was developed to support high-accuracy wave-front interferometry of EUV optical systems [18,19]. With an electron beam of elliptical cross-section, having a vertical size $d_v = 2\sigma_v = 32 \mu\text{m}$, and an emission half-angle $\theta = 80 \mu\text{rad}$ (the central radiation cone containing a $1/N$ relative spectral bandwidth, where N is the number of magnet periods of the undulator [6].), the product $d \cdot \theta$ is just slightly larger (20%) than $\lambda/2\pi$ at the 13.4 nm wavelength used in these experiments. Thus we expect to see strongly correlated fields, of high spatial coherence, in the vertical plane. The horizontal beam size is considerably larger with $d_h = 2\sigma_h = 520 \mu\text{m}$, so that with approximately the same emission half-angle we expect it to be spatially coherent over only a fraction of the horizontal extent of the radiated beam.

The coherence characterization presented here is performed at the focus of the condenser system used

to re-image the undulator source to the entrance of our experimental chamber. In the case of beamline 12, this condenser is a Kirkpatrick–Baez (KB) system [6]. Its focal plane serves as the entrance plane for various experiments, including EUV phase-shifting point diffraction interferometry [18,19]. The coherence measurement is based on an implementation, at a shorter wavelength, of the well known Thompson and Wolf two-pinhole experiment [2]. The Thompson and Wolf experiment is essentially an extension of Young's classic two-slit interference experiment [1], where in this case fringe visibility is recorded as a function of pinhole separation in order to determine the spatial coherence properties of the illuminating beam. Under the conditions that: (1) the pinholes are small enough such that the field within each pinhole can be regarded as constant, (2) the bandwidth of the illuminating beam is narrow enough that temporal coherence does not significantly affect fringe visibility, and (3) the intensity at the two sampled points are equal, the fringe visibility can be shown to be proportional to the magnitude of the complex coherence factor, μ , [3,4]. Typical measured interference patterns are presented in Fig. 2, which shows interference modulation of the Airy envelope as a function of pinhole separation distance. These patterns provide a direct measure of the spatial coherence of undulator radiation as transported by the beamline optical system.

2. Experiment

The experimental system is depicted in Fig. 1. The beamline [17] provides an overall 60:1 demagnified image of the source in the focal plane of the KB system. The undulator employed at this beamline has a magnet period (λ_u) of 8 cm, 55 magnet periods (N), and a non-dimensional magnetic field parameter $K = 2.7$. The electron beam energy is 1.9 GeV, with a corresponding relativistic Lorentz factor $\gamma = 3720$. The acceptance half-angle (NA) of undulator radiation for these experiments is set by the acceptance aperture of the beamline, which is a 1.6 mm diameter circle placed 16.7 meters downstream of the undulator exit. This acceptance NA of $48 \mu\text{rad}$ is somewhat smaller than the central radiation cone

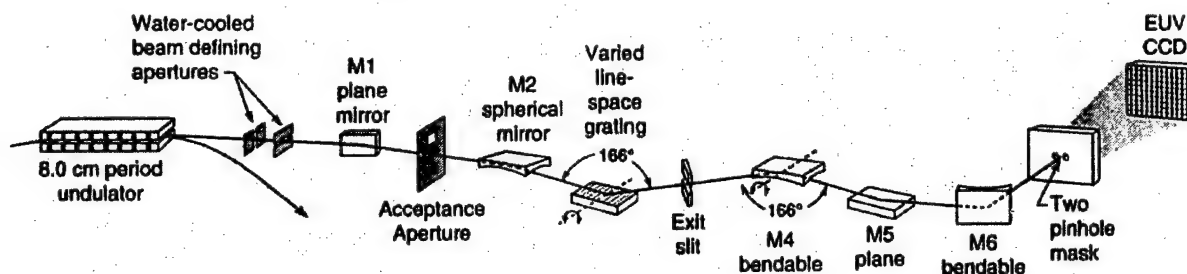


Fig. 1. The experiment setup shows the undulator, beamline optics, monochromator grating and exit-slit, Kirkpatrick–Baez (KB) re-focusing optics (M4 and M6), and the spatial coherence measuring end-station consisting of a two-pinhole mask and an CCD electronic array detector. The two pinholes are shown here with a horizontal separation; vertical separation tests are also employed.

half-angle, $\theta_{\text{cen}} = \sqrt{1 + K^2/2} / \gamma\sqrt{N} = 80 \text{ } \mu\text{rad}$ [6,17]. The radiation within θ_{cen} has a natural bandwidth of $\lambda/\Delta\lambda = N$, corresponding to a longitudinal coherence length, l_{coh} , of $0.37 \text{ } \mu\text{m}$. The monochromator bandpass of this beamline can be narrowed to values as large as $\lambda/\Delta\lambda = 1100$, by adjusting the size of its horizontal exit-slit. Except where stated otherwise, all experiments reported in this paper were performed with the monochromator exit-slit set such as to pass the entire $\lambda/\Delta\lambda = 55$ natural undulator bandwidth. Accounting for the $48 \text{ } \mu\text{rad}$ acceptance NA, the spatially coherent power is expected to be about 12 mW, within a relative bandwidth of $\lambda/\Delta\lambda = 55$ at $\lambda = 13.4 \text{ nm}$ [17]. Using the full $80 \text{ } \mu\text{rad}$ acceptance NA defined by θ_{cen} would yield expected coherent power of 30 mW. This bandwidth is sufficient to assure that the quasi-monochromatic condition required for this experiment is satisfied, i.e. that the temporal coherence does not significantly affect fringe visibility.

As shown in Fig. 1, the M2 spherical mirror images the undulator output vertically to the monochromator exit-slit. The calculated FWHM of the vertical intensity profile on the exit-slit is $17 \text{ } \mu\text{m}$, neglecting aberrations on M2 mirror. The KB system is composed of two asymmetric, bendable reflective mirrors (M4 and M6). Mirror M6 directly demagnifies the undulator source in the horizontal direction by a factor of 60, whereas M4 demagnifies the monochromator exit-slit in the vertical direction by a factor of 7.2. M2 and M4 together provide a total vertical demagnification of 60 in the plane of the two-pinhole mask.

To implement these coherence tests, a patterned mask containing multiple 450 nm -diameter-pinhole

pairs, with separations ranging from 1 to $9 \text{ } \mu\text{m}$, was placed in the vicinity of the KB system focus, i.e. at the demagnified image of the undulator source. The 450 nm pinhole diameter is chosen to be significantly smaller than the expected coherence width, while providing reasonable throughput and appropriate working distance for full Airy pattern recording at the charge-coupled-device (CCD) electronic array detector. The mask, fabricated using electron-beam lithography and reactive-ion etching, consists of a 360 nm -thick Ni absorbing layer evaporated on a 100 nm -thick Si_3N_4 membrane. The mask features are etched completely through the membrane prior to the Ni evaporation, leaving the pinholes completely open in the finished mask. Pinhole circularity and size are confirmed by observing the resultant far field Airy patterns, as recorded on an the CCD.

The pinhole array mask is mounted on an x - y - z stage, allowing desired pinhole separations to be selected sequentially, and the coherence to be studied as a function of focal position. A back-thinned, back-illuminated, EUV sensitive CCD camera is placed 26 cm downstream of the mask to record the resulting interference pattern. The active area of the CCD is $25.4 \text{ mm} \times 25.4 \text{ mm}$, in a 1024 by 1024 pixel array. Typical exposure times for a recorded pattern vary between 50 ms and 5 s depending on pinhole separation, storage ring current, and beam-line apertures.

Because the divergence created by the pinhole diffraction is large relative to the pinhole separation, the two diffraction patterns overlap to a high degree on the CCD. In order to determine the magnitude of the complex coherence factor, μ , from the fringe visibility, we must know the relative intensities of

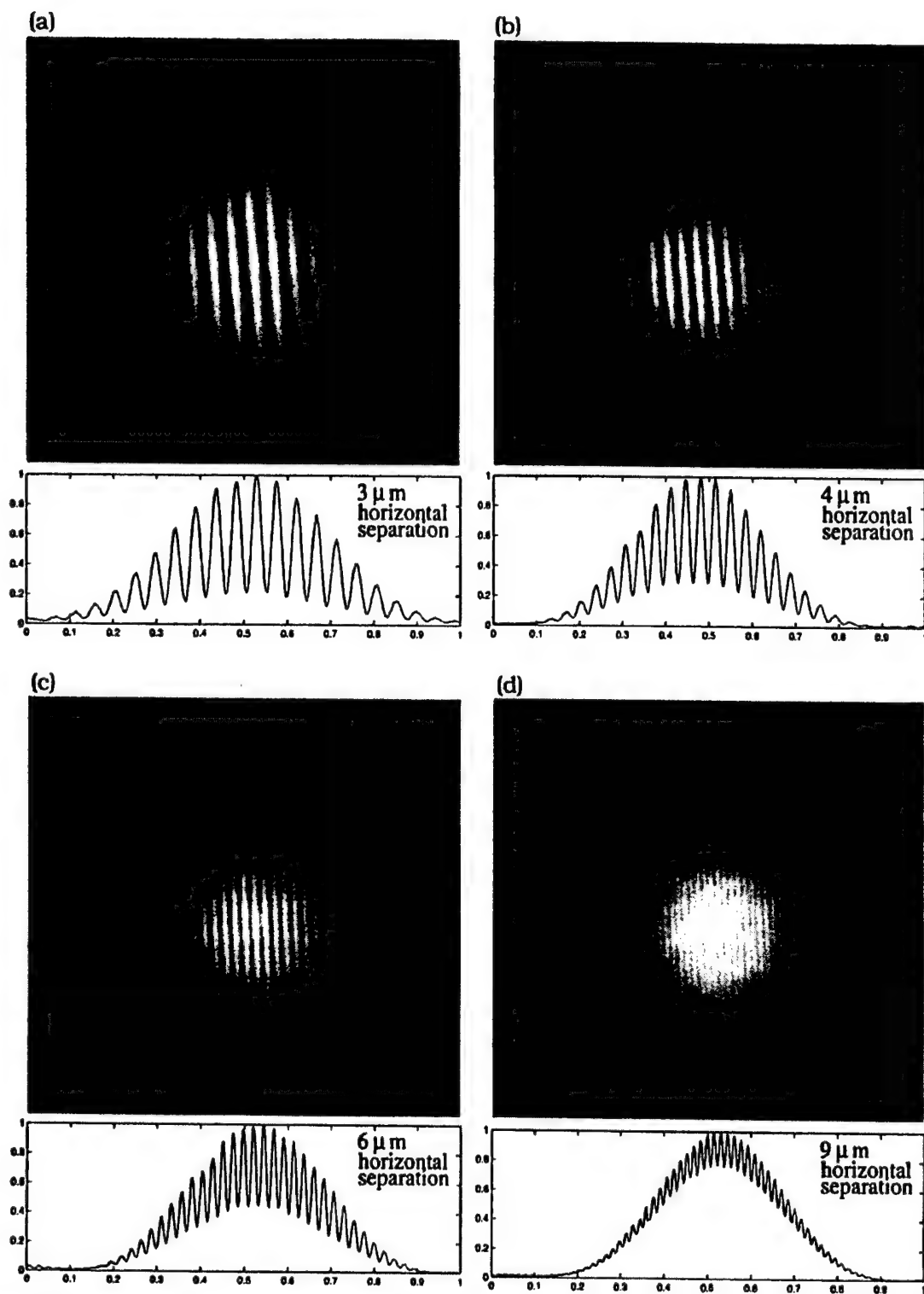


Fig. 2. Measured two-pinhole interference patterns for horizontal pinhole separations of 3, 4, 6 and 9 μm , for a wavelength of 13.4 nm and a beamline acceptance half-angle of 48 μrad . The pinhole diffraction patterns overlap and produce an interference pattern within the Airy envelope. The interference patterns are recorded on an EUV sensitive CCD camera, located 26 cm downstream of the pinhole mask. Pinhole diameter range from 400 to 500 nm, but are equal in their respective pairs. As shown in the lineouts, fringe visibility of the modulation decreases for larger separations. Spectral resolution for these measurements is 55.

the illuminating beam at the two pinholes or, alternatively, guarantee them to be equal. This can be

challenging as the pinholes are near the KB focal plane, where the beam is small and may display

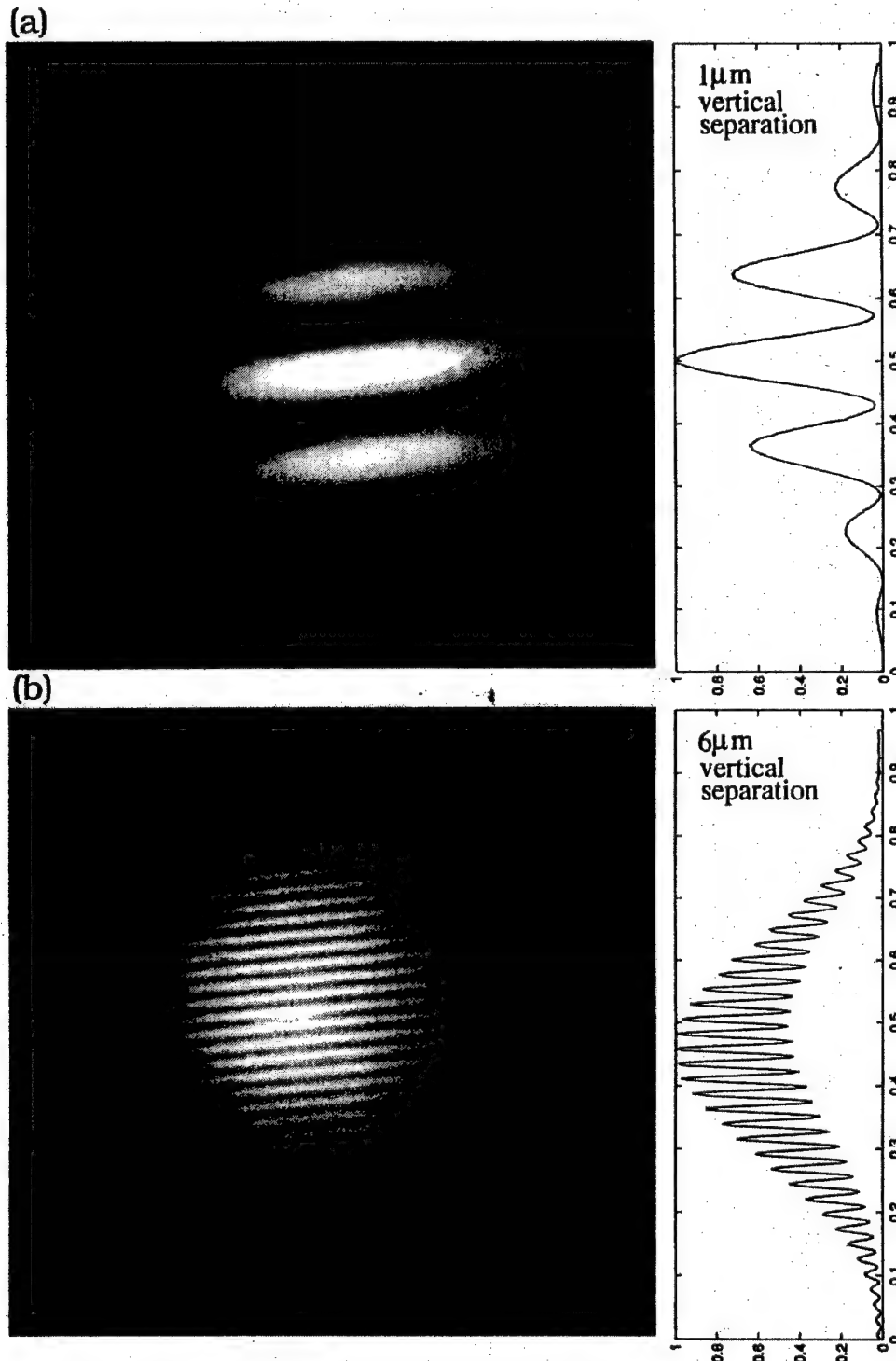


Fig. 3. Measured two-pinhole interference patterns for vertical pinhole separations of 1 and 6 μm , a wavelength of 13.4 nm, and an acceptance half-angle of 48 μrad .

structure due to aberrations in the optics. Because it is impractical to independently measure the intensity at each pinhole, we attempt to guarantee the equal intensity condition by performing a large ensemble (greater than 50) of measurements for each pinhole separation, intentionally displacing the pinhole pair relative to the incident beam. Because beam-intensity non-uniformity can only degrade fringe visibility, we take the highest fringe visibility from the ensemble of measurements as representing the coherence-limited fringe visibility.

Fig. 2 shows the recorded interference patterns for horizontal pinhole separations of 3, 4, 6 and 9 μm . The measured magnitude of the fringe visibility decreases with larger pinhole separation as expected. Fig. 3 shows several interference patterns obtained with vertically displaced pinhole pairs. Fringe modulation is generally better than that of horizontally displaced pinholes. In order to verify our ability to control and measure the beamline coherence properties, the measurement was repeated at a larger beamline acceptance NA. This NA can be controlled by way of the acceptance aperture described above. The measured spatial coherence decreases in both directions as expected when the 48 μrad acceptance aperture is replaced by a larger aperture allowing the entire 80 μrad central radiation cone to pass.

The interference pattern at the CCD can be written as [4]

$$I(x, y) = 2I^{(1)}(x, y) \left[1 + \mu \cos \left(\frac{2\pi}{\lambda z} sx + \phi \right) \right], \quad (3)$$

where $I^{(1)}(x, y)$ is the Airy intensity envelope in the recording plane due to pinhole diffraction, x is the axis on the recording plane that is parallel to the pinhole separation, s is the pinhole separation, λ is the wavelength, and z is the distance from the pinholes to the recording plane. Note that the phase ϕ describes the fringe shift relative to the geometric center of the interference pattern. With equi-phase illumination of the two pinholes and proper pinhole alignment, $\phi = 0$. Because fringe visibility is defined as

$$\mathcal{V} \equiv \frac{I_{\max} - I_{\min}}{I_{\max} + I_{\min}}, \quad (4)$$

we have $\mathcal{V} = \mu$ as a constant over the entire interferogram for the cases considered here.

To obtain the fringe visibility from the interference pattern, we perform a two-dimensional Fourier transform of the interferogram and separate the ze-

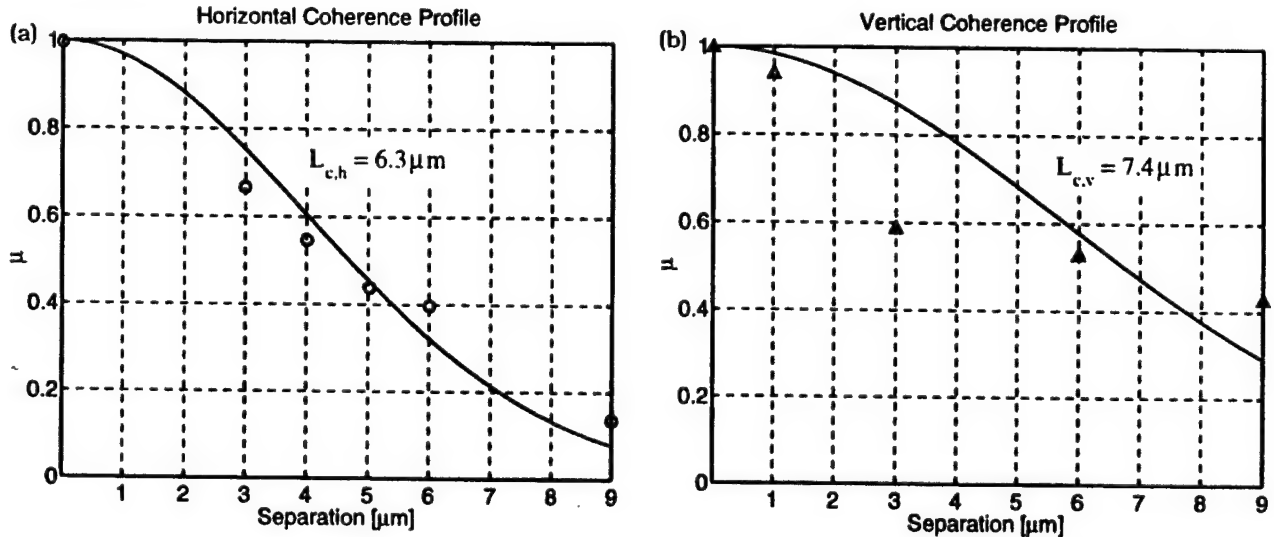


Fig. 4. The measured coherence factor μ as function of pinhole separation distance for (a), horizontally and (b), vertically separated pinholes. For these measurements, a 48 μrad half-angle acceptance aperture is used. The measured spatial coherence distance decreases with larger pinhole separations as expected. Larger uncertainty in the vertical 3 μm separation may be due to a smaller number of interferograms collected in this case. The data points are fitted to a Gaussian curve in each case.

roth order and the two first-order peaks. As seen in Eq. (3), the Fourier transform of the interferogram $I(x, y)$ can be represented as the convolution of the Fourier transform of the Airy envelope with three delta functions. The delta functions arising from the $1 + \cos(\cdot)$ term can be written as

$$\delta(f_x, f_y) + \frac{\mu}{2} \left[\delta\left(f_x + \frac{s}{\lambda z}, f_y\right) + \delta\left(f_x - \frac{s}{\lambda z}, f_y\right) \right].$$

Furthermore, the Fourier transform of the Airy envelope becomes the autocorrelation of the pinhole. The resultant pattern in the frequency domain is therefore one zeroth order peak and two symmetric first-order peaks, each properly scaled. Ideally, the fringe visibility is two times the relative strength of the first-order peak to the zeroth-order peak. In practice, we apply properly displaced top-hat filters centered at each peak and integrate within the filters. The fringe visibility is then determined by two times the ratio of the integration under the first-order peak to that under the zeroth-order peak.

In Fig. 4 we show μ as a function of pinhole separation for both horizontally and vertically separated pinholes. One observes that the transverse coherence distance in the vertical plane is greater than that in the horizontal plane, for this 48 μrad acceptance NA. Following the convention in [4], a transverse coherence distance L_c for the measured coherence profiles (Fig. 4) is obtained by determining the width of an equivalent top-hat function, i.e.,

$$L_c \equiv \int_{-\infty}^{\infty} |\mu(\Delta x)|^2 d\Delta x. \quad (5)$$

The measured transverse coherence distance in the horizontal direction, $L_{c,h}$, is found to be approximately 6.3 μm and the measured transverse coherence distance in the vertical direction, $L_{c,v}$, is found to be approximately 7.4 μm . This is due to the fact that the vertical source dimension is sub-resolution in size at this acceptance angle, while the horizontal

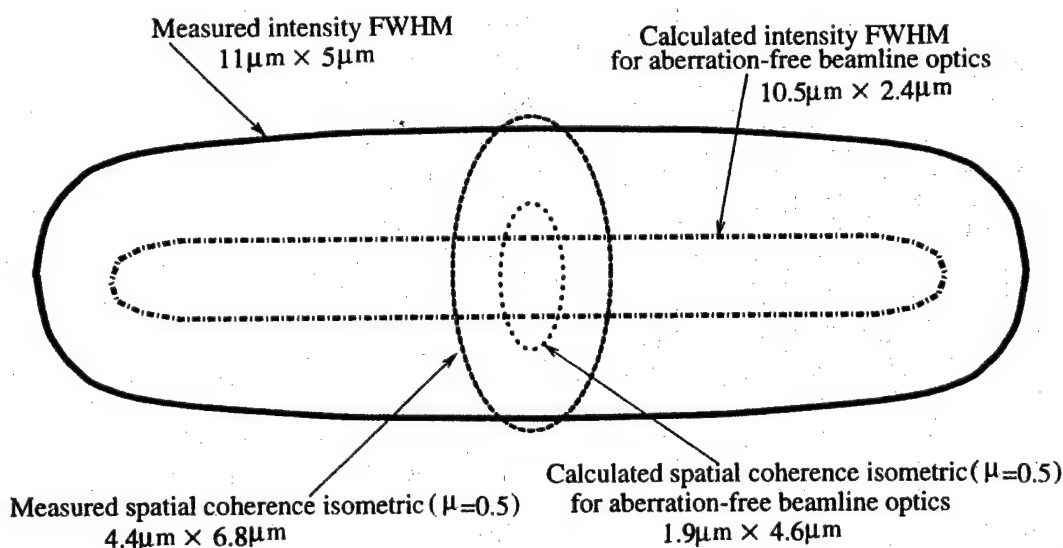


Fig. 5. The beamline is designed to image the undulator output to the KB focus with a demagnification of 60 and an acceptance half-angle of 48 μrad . The undulator output in this calculation is assumed to be a monochromatic ($\lambda = 13.4 \text{ nm}$), spatially incoherent Gaussian-shaped source with $(\sigma_x, \sigma_y) = (260 \text{ } \mu\text{m}, 16 \text{ } \mu\text{m})$ [6], corresponding to source plane values of 612 $\mu\text{m} \times 38 \text{ } \mu\text{m}$ FWHM. The solid line shows the FWHM of the measured KB focal intensity distribution. The dash-dot line is the FWHM of this calculated KB focal intensity distribution assuming an aberration-free beamline. The intensity distribution FWHM values are increased by aberrations from ideal values of 10.5 $\mu\text{m}(H) \times 2.4 \text{ } \mu\text{m}(V)$, to experimental values of 11 $\mu\text{m}(H) \times 5 \text{ } \mu\text{m}(V)$. The dashed line represents the calculated focal plane spatial coherence isometric ($\mu = 0.5$) for experimental values of wavelength, acceptance NA, and demagnification, as calculated using the van Cittert–Zernike theorem [3,4]. The asymmetric coherence isometric is due to the asymmetry of the source intensity distribution.

size is not ¹. After propagating from the undulator exit (source), the FWHM of the spatial coherence profile, as calculated by the van Cittert–Zernike theorem, is 0.3 mm(*H*) × 5.2 mm(*V*) at the beamline acceptance aperture. Therefore, the spatial coherence profile at the KB focal plane (image plane) is expected to be asymmetric with vertical coherence better than horizontal coherence.

The effect of radiation directly transmitted through the mask membrane, a source of noise in these measurements, can be seen in Fig. 2(d). This effect becomes more significant as the pinhole separation increases because the limited beam size (see Fig. 5) results in a reduced illumination intensity at each pinhole, whereas the directly transmitted radiation remains fixed. This directly transmitted light adds a background noise to the interference pattern, thus reducing fringe visibility locally in the affected region. Therefore, when applying the Fourier transform method to the cases of large pinhole separations, we avoid the region containing directly transmitted light. This Fourier transform method has the advantage of evaluating the fringe visibility as an integrated, rather than localized, property of the full interferogram.

The intensity and coherence distribution in the KB focal plane is calculated by way of computer simulation for an aberration-free beamline. The simulation shows that the coherence profile is wider than the calculated intensity profile for the aberration-free beam in the vertical direction, which means that without aberrations the beam would be essentially fully coherent in the vertical direction. Horizontally, the coherence profile is dominated by the acceptance NA. As described above, this asymmetry is expected based on the geometry of the system.

Fig. 5 displays both FWHM intensity contours and $\mu = 0.5$ isometrics for both the aberration-free simulation case, and the actual measured results. In

both cases the vertical coherence is seen to be larger than the beam vertical FWHM, indicating nearly complete coherence in the vertical direction. Also both simulation and experiment show the horizontal coherence to be smaller than the vertical coherence and significantly smaller than the beam. This is a result of the extended source in the horizontal direction and the beamline geometry. The results differ, however, in that the measured coherence and beam-size are larger than those predicted for the aberration-free simulation. The beam-size increase is attributed to aberrations in the KB. By comparing the two intensity profiles we surmise the aberration limited point-spread function of the KB to be about 4 μm in diameter. We assume these aberrations to also play a role in the increased coherence observed experimentally.

2.1. Effect of monochromator exit-slit

The natural bandwidth of undulator radiation within the central radiation cone, θ_{cen} , is set by the number of magnet periods *N*, which is 55 in these experiments. The monochromator is designed to transmit a bandpass variable from $\lambda/\Delta\lambda = 55$ to 1100. The larger value is useful in experiments requiring a longer coherence length (to 7.4 μm at 13.4 nm wavelength). These values of spectral bandpass correspond to exit-slit widths of 320 μm and 16 μm , respectively. Exit-slit size greater than 320 μm does not further affect the monochromator bandpass. All data presented to this point correspond to a 400 μm exit-slit size ($\lambda/\Delta\lambda = 55$). Use of a smaller monochromator exit-slit narrows the transmitted spectrum, but also has the effect of decreasing the transmitted beam's transverse phase-space, and thus increasing the spatial coherence length in the vertical plane. To study the effect of the monochromator exit-slit size, we have repeated the experiment with exit-slit size as a parameter. Fig. 6 shows the measured horizontal and vertical coherence as a function of monochromator exit-slit size. For a vertical pinhole separation of 6 μm , the fringe visibility varies from 0.38 to 0.94 as the exit-slit size changes from 400 μm to 50 μm . For the horizontally oriented 4 μm separation pinholes, the fringe visibility varies from 0.47 to 0.60 as the exit-slit size changes from

¹ Simple analysis of a critical illumination system like the one considered here would suggest the coherence to be symmetric when the NA is symmetric. More detailed analysis reveals, however, that the small vertical source size causes the vertical coherence width at the entrance pupil to be large relative to the pupil size. In this case we violate the assumptions typically used for predicting coherence in a critical illumination. This causes a preferential increase of coherence in the vertical direction.

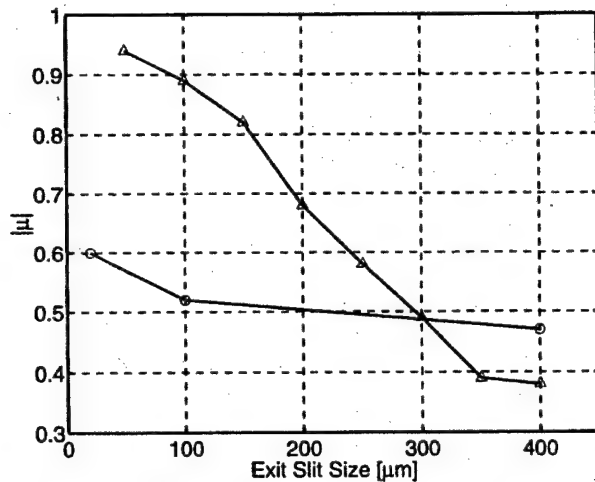


Fig. 6. The vertical opening of monochromator's exit-slit has significant effect on the vertical coherence but not on the horizontal coherence. A smaller exit-slit size decreases the vertical phase-space of the transmitted radiation, thus increasing the vertical coherence. Horizontal coherence is relatively unaffected. This is done with a larger beamline acceptance NA.

400 μm to 20 μm . As one expects, the exit-slit also acts as a spatial filter, having a significant effect on

spatial coherence in the vertical plane, and minimal effect in the horizontal plane.

2.2. Wave-front null test

The two-pinhole experiment presented here can also be used to measure the departure from sphericity of the pinhole-diffracted wave. Fig. 7 is derived from the measured interference pattern obtained with 450 μm diameter pinholes horizontally placed 9 μm apart. To determine the underlying wave-front quality of the two nearly spherical waves used to produce the interference pattern, the interferogram is analyzed using conventional Fourier-transform wave-front reconstruction techniques routinely applied to carrier-frequency interferograms [20]. The resulting wave-front is then compared to what one would expect from two perfectly spherical waves in our recording geometry. The rms departure from a sphere is taken to represent the underlying pinhole-diffracted wave-front quality. For example, at a numerical aperture of 0.025 (a typical input numerical aperture for testing EUV optics), the wave-front

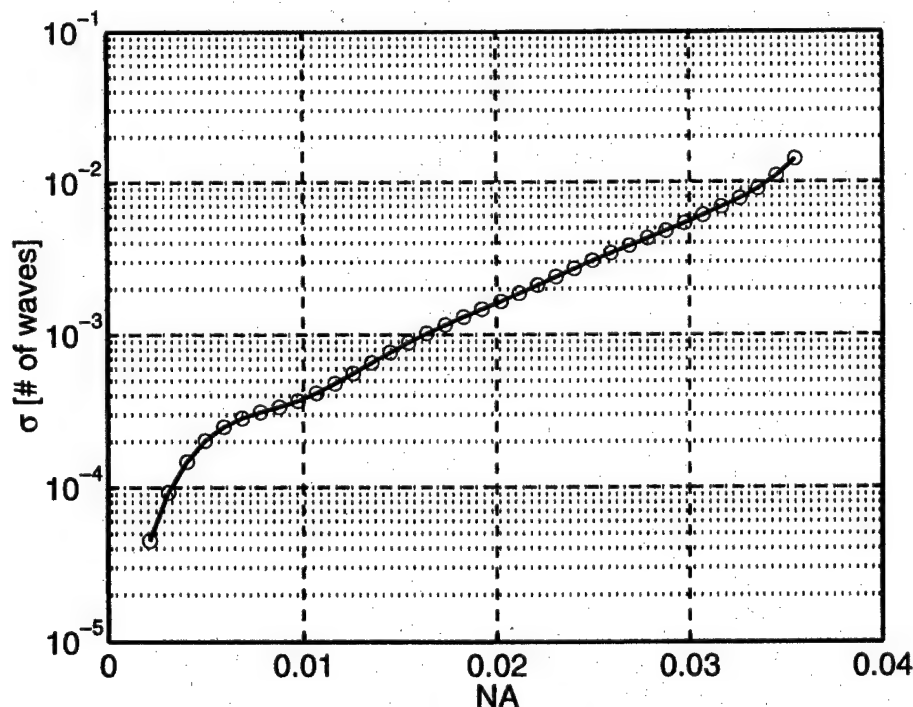


Fig. 7. Departure of pinhole generated wave-front from sphericity, expressed as an rms number of waves at $\lambda = 13.4$ nm. For example, the data indicates that with 450 nm-pinhole filtered radiation a wave-front departure from a sphericity of $\lambda/1000$ is obtained across a wave-front of about 0.016 NA (equal to 13 picometer rms at this wavelength and NA).

quality from these 450 μm pinholes is seen to be $\lambda/330$, exceeding current requirements for such tests [18,19].

3. Conclusion

The coherence properties of spatially filtered undulator radiation have been measured. A very high degree of spatial coherence is demonstrated, as expected on the basis of a simple model. The effect of an asymmetric source size on the resultant coherence properties is observed, and is consistent with aperturing within the beamline optical system used to transport radiation to the experimental chamber. Based on these observations and well understood scaling of undulator radiation, it is evident that high average power, spatially coherent radiation is available at modern storage rings with the use of appropriate pinhole spatial filtering techniques.

Acknowledgements

The authors would like to thank Dr. Kenneth Goldberg for valuable discussion. Special thanks are due to the entire CXRO engineering team and most notably to Phil Batson, Paul Denham, Drew Kemp and Gideon Jones for bringing the experimental hardware to fruition. This work was supported in part by the Office of Basic Energy Sciences, Department of Energy, by DARPA's Advanced Lithography Program, by the Air Force Office of Scientific Research, by Intel Corporation, and by the Extreme Ultraviolet Lithography Limited Liability Corporation.

References

- [1] T. Young, *Lectures on Natural Philosophy I*, London, 1807, 464.
- [2] B.J. Thompson, E. Wolf, *J. Opt. Soc. Am.* 47 (1957) 895.
- [3] M. Born, E. Wolf, *Principles of Optics*, Cambridge University Press, Cambridge UK, 1999, seventh edition.
- [4] J.W. Goodman, *Statistical Optics*, Wiley, New York, 1985.
- [5] N. Bloembergen, *IEEE J. Quantum Electron.* 20 (1984) 556.
- [6] D.T. Attwood, *Soft X-Rays and Extreme Ultraviolet Radiation*, Cambridge University Press, Cambridge UK, 1999, chapters 5 and 8.
- [7] D. Attwood, K. Halbach, K.-J. Kim, *Science* 228 (1985) 1265.
- [8] R. Coisson, *Appl. Optics* 34 (1995) 904.
- [9] A. Kondratenko, A. Skrinsky, *Opt. Spectrosc.* 42 (1977) 189. While not specifically addressing undulator radiation, this paper points out the essence of spatially coherent radiation from relativistic electrons.
- [10] Y. Takayama, R.Z. Tai, T. Hatano, T. Miyahara, W. Okamoto, Y. Kagoshima, *J. Synchro. Radiat.* 5 (1998) 456.
- [11] D.L. Abernathy, G. Gruebel, S. Brauer, I. McNulty, G.B. Stephenson, S.G.J. Mochrie, A.R. Sandy, N. Mulders, M. Sutton, *J. Synchro. Radiat.* 5 (1998) 37.
- [12] Z.H. Hu, P.A. Thomas, A. Snigirev, I. Snigireva, A. Souvorov, P.G.R. Smith, G.W. Ross, S. Teat, *Nature* 392 (1998) 690.
- [13] M.C. Marconi, J.L.A. Chilla, C.H. Moreno, B.R. Benware, J.J. Rocca, *Phys. Rev. Lett.* 79 (1997) 2799.
- [14] C. Spielmann, H. Burnett, R. Sartania, R. Koppitsch, M. Schnurer, C. Kan, M. Lenzner, P. Wobrauschek, F. Krausz, *Science* 278 (1998) 661.
- [15] D. Schulze, M. Dorr, G. Sommerer, J. Ludwig, P.V. Nickles, T. Schlegel, W. Sandner, M. Drescher, U. Kleineberg, U. Heinzmann, *Phys. Rev. A* 57 (1998) 3003.
- [16] A recent *Nature News in Brief*, 02 Mar. 2000, report describes the shortest wavelength FEL to date, <100 nm, achieved at the Deutsches Elektronen-Synchrotron (DESY) in Hamburg. The following review article describes preparation for those experiments: H. Nuhn, J. Rossbach, J. The challenge to be overcome to produce the ultimate x-ray source – the x-ray laser. *Synchrotron Radiation News* 13 (2000) 18.
- [17] D. Attwood, P. Naulleau, K. Goldberg, E. Tejnill, C. Chang, R. Beguiristain, P. Batson, J. Bokor, E.M. Gullikson, M. Koike, H. Medeck, J.H. Underwood, *IEEE J. Quantum Electron.* 35 (1999) 709.
- [18] P. Naulleau, K.A. Goldberg, S.H. Lee, C. Chang, D. Attwood, J. Bokor, *Appl. Optics* 38 (1999) 7252.
- [19] K. Goldberg, P. Naulleau, J. Bokor, *J. Vac. Sci. Technol. B* 17 (1999) 2982.
- [20] M. Takeda, H. Ina, S. Kobayashi, *J. Opt. Soc. Am.* 72 (1982) 156.

Achievement of essentially full spatial coherence in a high-average-power soft-x-ray laser

Y. Liu,^{1,4} M. Seminario,² F. G. Tomasel,² C. Chang,^{3,4} J. J. Rocca,² and D. T. Attwood,^{1,3,4}¹Applied Science and Technology Graduate Program, University of California, Berkeley, California 94720²Department of Electrical and Computer Engineering, Colorado State University, Fort Collins, Colorado 80523³Department of Electrical Engineering and Computer Science, University of California, Berkeley, California 94720⁴Center for X-ray Optics, Lawrence Berkeley National Laboratory, Berkeley, California 94720

(Received 21 July 2000; published 5 February 2001)

We report an observation of essentially full spatial coherence in a high average power soft-x-ray laser. Rapid coherence buildup due to strong refractive antiguiding in a long plasma column is experimentally demonstrated. This allows the generation of fully coherent, milliwatt-level average power soft-x-ray radiation by a tabletop device. The peak brightness of this laser reaches 2×10^{25} photons s^{-1} mm^{-2} $mrad^{-2}$ within 0.01% spectral bandwidth, making it one of the brightest soft-x-ray sources available.

DOI: 10.1103/PhysRevA.63.033802

PACS number(s): 42.55.Vc

Applications such as high-resolution microscopy, interferometry, lithography, and holography motivate the development of advanced light sources at soft-x-ray wavelengths. Current approaches for the generation of high brightness coherent radiation in this spectral region include undulators at modern synchrotron radiation (SR) facilities [1], high-order harmonic generation (HHG) of optical lasers [3,4], and soft-x-ray lasers [2]. The degree of spatial coherence of radiation plays a critical role in many of the most important applications. For SR sources, high spatial coherence is achieved at the expense of photon flux by spatial filtering [1]. HHG sources driven by coherent optical lasers have shown high spatial coherence with average powers reaching the order of microwatts by using a phase-matching technique [4]. Compared with SR and HHG sources, soft-x-ray lasers have substantially higher pulse energy and narrower linewidth. However, to date they have been characterized by rather low spatial coherence [5–9]. The demonstration of nearly full spatial coherence has been one of the main goals of soft-x-ray laser research.

Soft-x-ray laser beams are generally limited to single-pass or double-pass amplification of spontaneous emission (ASE) through the plasma. From the van Cittert–Zernike theorem [10], a high degree of spatial coherence from an ASE-based laser can be achieved when the gain medium has a Fresnel number less than unity. However, this is difficult to achieve in a plasma column, unless some forms of spatial filtering are used [11,12]. Here we experimentally demonstrate that refraction in a plasma with sharp density gradients can reduce the effective transverse source size significantly and result in essentially full spatial coherence. Although theoretical results have suggested that refractive antiguiding and gain guiding along a long plasma column could result in improved spatial coherence [13–15], in previous experiments the coherence buildup was limited to values significantly below full coherence [7,16]. In the present work, we utilized fast capillary discharge excitation to produce plasma columns with both very high axial uniformity and the length-to-diameter ratio exceeding 1000:1, in which strong refractive antiguiding makes it possible to achieve essentially full spatial coherence with a plasma column length of 36 cm.

The laser beam in our experiments is generated by excitation of an Ar-filled capillary channel with a fast discharge current pulse that rapidly compresses the plasma to form a dense and hot column with a large density of Ne-like ions [17,18]. Collisional electron impact excitation of the Ne-like ions produces a population inversion between the $3p(^1S_0)$ and $3s(^1P_1^o)$ levels, resulting in amplification at 46.9 nm. The experiments are conducted utilizing aluminum oxide capillary channels 3.2 mm in diameter and up to 36 cm in length, filled with preionized Ar gas at a pressure of ~ 59 Pa. The plasma columns are excited by current pulses of ~ 25 kA peak amplitude, with a 10–90% rise time of approximately 40 ns. The setup is similar to that used in previous experiments [19,20]. The excitation current pulse was produced by discharging a water dielectric capacitor through a spark gap switch connected in series with the capillary load. The laser is very compact and occupies a table area of only 0.4×1 m². Efficient extraction of energy is obtained by operating the laser in a highly saturated regime. The laser pulse energy increases nearly exponentially as a function of plasma column length, until the beam intensity reaches the gain saturation intensity at a plasma column length of about 14 cm [18]. For longer plasma columns, the laser average pulse energy increases linearly with length from 0.075 mJ for a plasma column 16 cm in length to 0.88 mJ ($> 2 \times 10^{14}$ photons/pulse) for a plasma column length of 34.5 cm [20]. Average laser powers of 3.5 mW are obtained when operating the laser at a repetition rate of 4 Hz.

The spatial coherence of a quasimonochromatic light

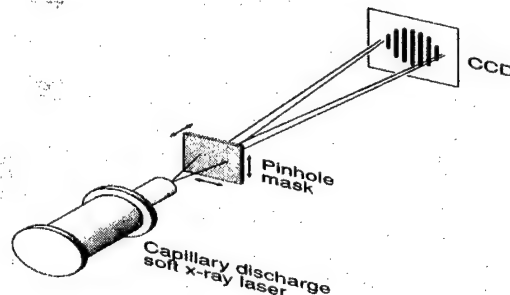
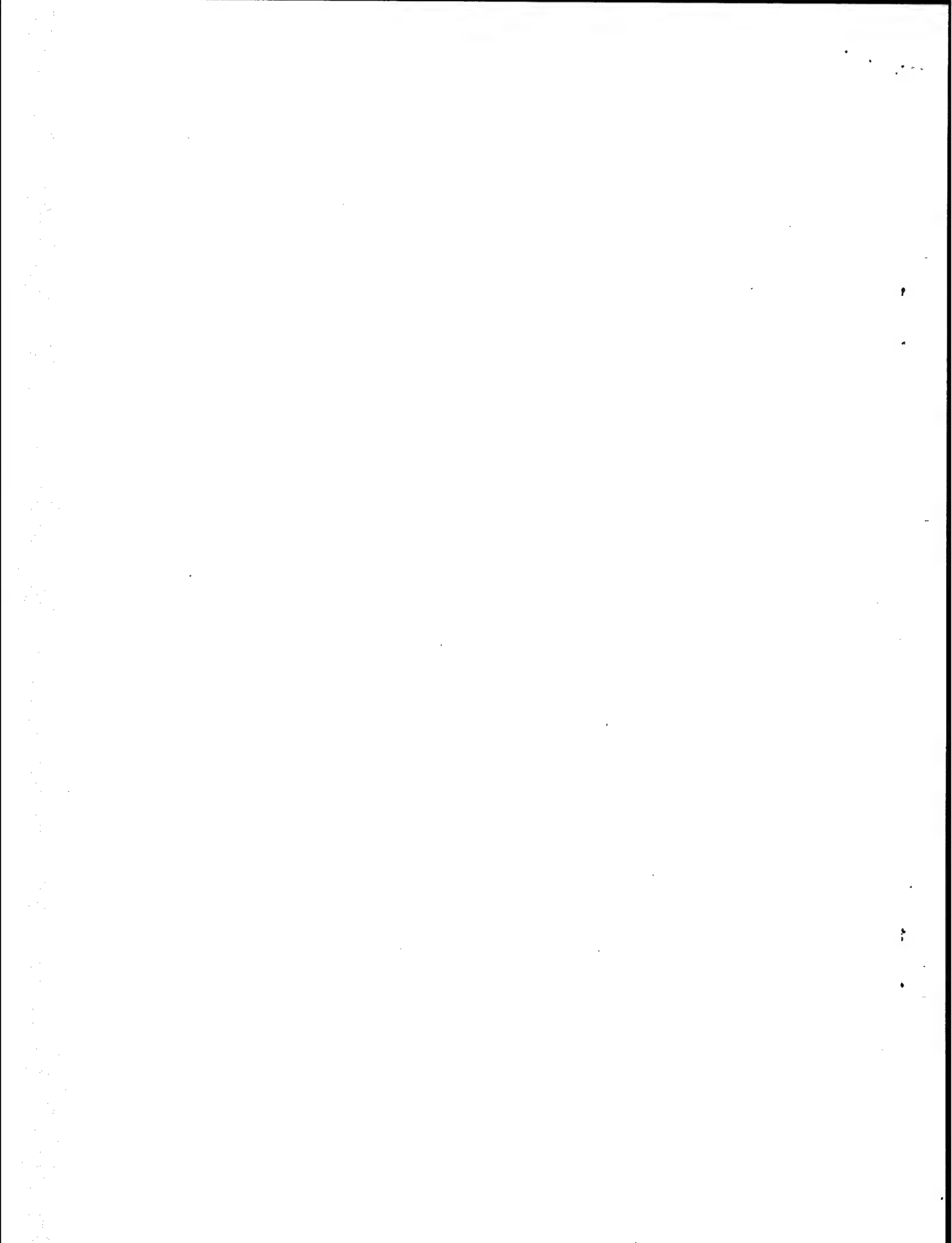


FIG. 1. Schematic representation of the experimental setup used in the two-pinhole interference coherence measurements.



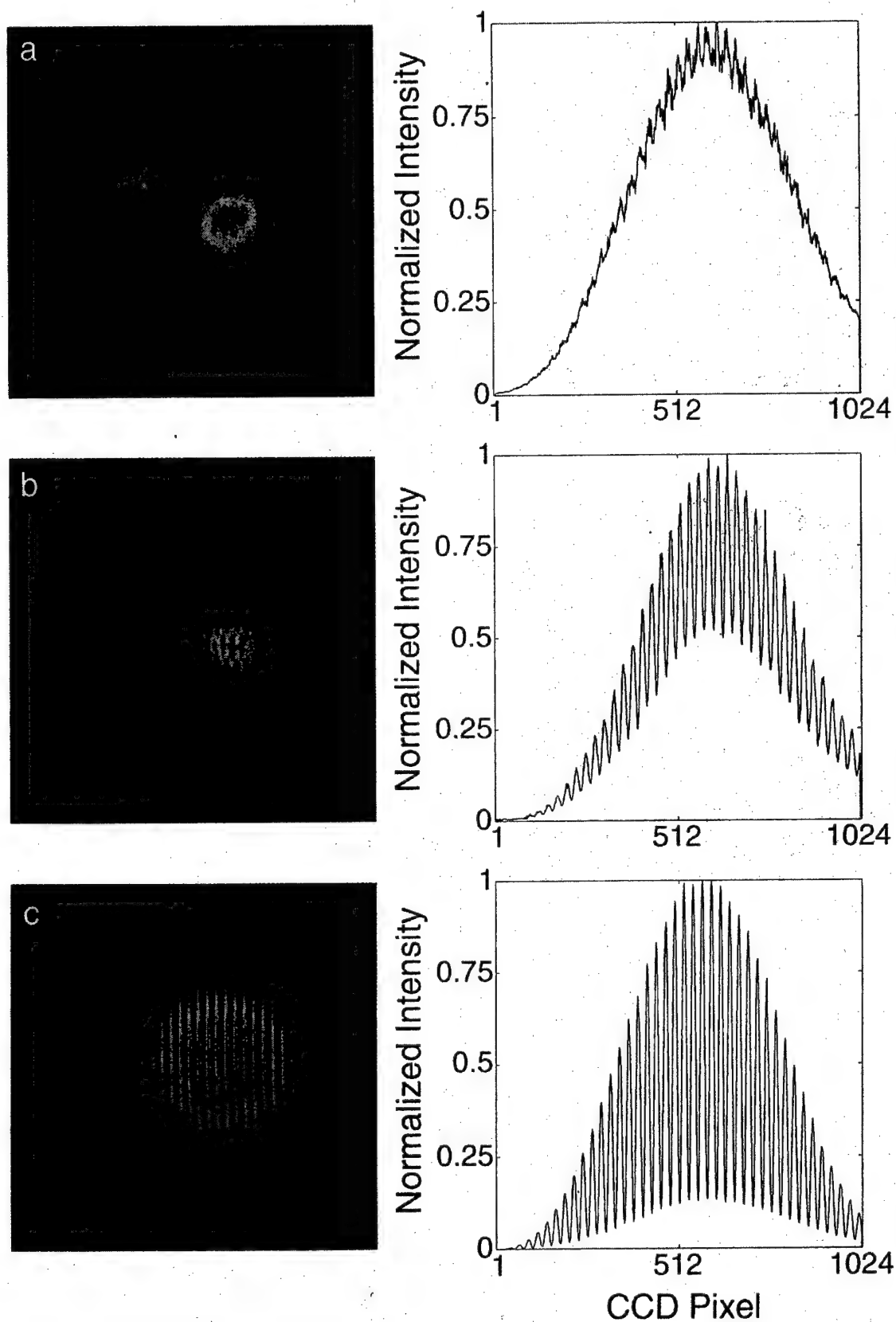


FIG. 2. (Color) Interferograms and their lineouts showing the coherence buildup of the laser beam with increasing capillary length. The capillary lengths are (a) 18, (b) 27, and (c) 36 cm. The lineouts are obtained by vertically integrating 15 pixels of the CCD images.

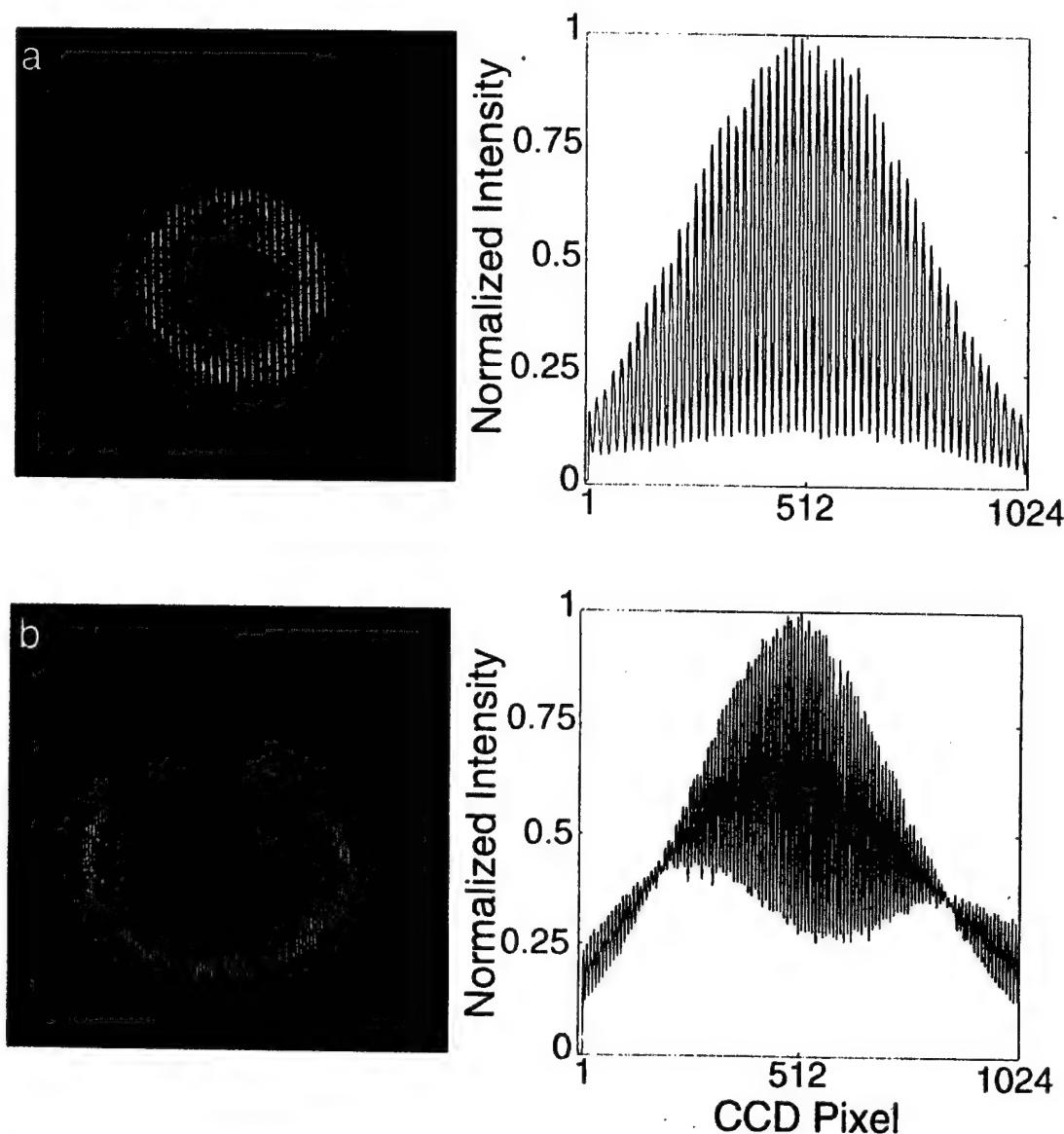


FIG. 3. (Color) Interferograms and their lineouts obtained with two pinholes located at 15.7 cm from the capillary exit. The pinhole separations are (a) 300 and (b) 680 μm .

source is characterized by the cross correlation of fields across the output wavefront, which can be described in terms of the normalized complex degree of coherence μ_{12} [10]. In a two-pinhole interference experiment, the fringe visibility, defined as $V = (I_{\text{max}} - I_{\text{min}}) / (I_{\text{max}} + I_{\text{min}})$, where I_{max} and I_{min} are the maximum and minimum intensities of the fringe pattern, as a function of pinhole separation is proportional to the modulus of μ_{12} [21]. This was demonstrated in experiments by Thompson and Wolf with partially coherent visible light [22]. Similar measurements were conducted recently in SR sources [23]. A variation of this method, a two-slit experiment, had been used in measuring the spatial coherence of both x-ray lasers [8,24] and HHG sources [25]. The laser used in our experiment has sufficiently high pulse energy for us to perform a two-pinhole interference experiment with a single laser pulse.

The setup used in our two-pinhole interference experiment is shown in Fig. 1. The pinhole masks consisted of

pairs of 10- μm -diam pinholes laser-drilled at selected separations on 12.5- μm -thick stainless-steel substrates (National Aperture Inc., NH). Measurements were conducted placing the masks at distances of 15 and 40 cm from the exit of the capillary. An x-y translation stage was used to position the pinholes with respect to the beam. The interference patterns were recorded with a thermoelectrically cooled, back-thinned charge-coupled device (CCD) having a 1024 \times 1024 pixel array (SI-003A, Scientific Imaging Technologies, Tigal, OR). The distance from the pinhole plane to the CCD was 300 cm. This distance was selected to assure that the CCD's spatial resolution (25- μm pixel size) is sufficient to resolve the finest interference fringes, while recording essential features of the pinhole diffraction patterns.

The interference patterns recorded by the CCD contain an underlying background that is due to spontaneously emitted radiation from the hot plasma. To reduce its effect, we recorded the background after acquiring each interferogram.

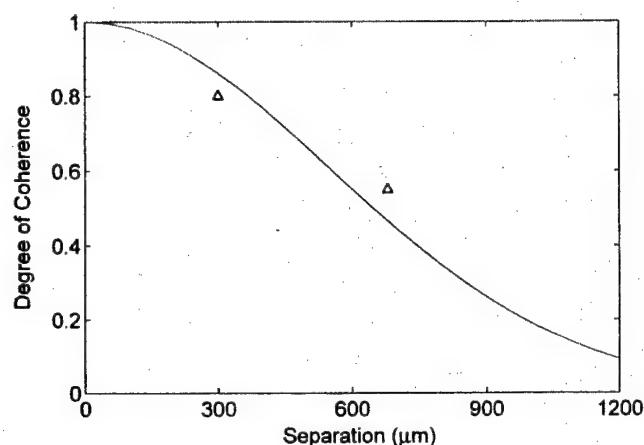


FIG. 4. Measured degree of coherence, $|\mu_{12}(\Delta x)|$, of the laser beam vs separation between two pinholes at 15.7 cm from the exit of the capillary. The solid line is for a Gaussian profile $|\mu_{12}(\Delta x)|$ with a coherence radius $R_c = 550 \mu\text{m}$.

This was done by increasing the gas discharge pressure to ~ 130 Pa, which quenches the laser line while maintaining the background emission. Final interferograms were obtained by subtracting the recorded backgrounds from the original interferograms. This procedure also removes thermal “dark counts” of the CCD. The background is, however, somewhat weaker in the higher pressure shots, thus the background removal is not complete. Therefore, the fringe visibility is always somewhat undervalued. As a result, the highest spatial coherence values reported herein, which are sensitive to a small amount of background, constitute a conservative evaluation of the spatial coherence of the source.

Comparative interferograms corresponding to increasing capillary lengths of 18, 27, and 36 cm are shown in Fig. 2, with their corresponding lineouts. A mask with a pinhole separation of $200 \mu\text{m}$ was used in all three measurements. The mask was positioned at a distance of 40 cm from the capillary exit. The interferograms consist of two almost entirely overlapped Airy patterns, modulated by the interference between them. The expected coherence buildup with increasing capillary length is clearly observed. The fringe visibility increases from 0.05 for the 18-cm-long capillary to 0.33 for the 27-cm-long plasma, and reaches 0.8 for the 36-cm capillary. Assuming a Gaussian profile $|\mu_{12}|$, the coherence radii [26] for the three capillary lengths are 80, 135, and $300 \mu\text{m}$, respectively. Although the last number is likely to be significantly underestimated as a result of the background error, it is quite clear that the coherence radius scales much faster than linearly with capillary length. This is evidence of refractive mode selection as gain guiding alone provides only a linearly increasing coherence radius [13,15].

Radiation traveling along a plasma tends to be refracted out of the central region, where the amplification process takes place. With the presence of strong refraction, only radiation that propagates near the axis experiences substantial gain and contributes to the output of the laser. Therefore, at the expense of the effective gain, refraction provides a mode-selection mechanism that improves the spatial coherence of soft-x-ray lasing. With the assistance of refraction, a coher-

ence radius comparable to the beam size was achieved with 36-cm-long capillary length. Evidence of near full spatial coherence requires measurements using pinholes with separation comparable to the beam size. To clarify the point, we positioned the pinholes closer (15.7 cm) to the capillary exit. The spatial profile of the laser beam at this position was previously measured [20] and verified during these experiments by scanning a single pinhole across the beam. Refraction causes a ring-shaped beam profile with a peak-to-peak diameter of approximately $950 \mu\text{m}$. Figures 3(a) and 3(b) show the obtained interferograms and their lineouts with pinhole separations of 300 and $680 \mu\text{m}$. In Fig. 3(a), visibility as high as 0.8 is observed. In Fig. 3(b), the large pinhole separation, combined with laser divergence, causes a large displacement of the two Airy patterns. The large visibility variations in different regions of the interferogram are the result of the intensity differences between the partially overlapped Airy patterns [21]. Maximum fringe visibility, ~ 0.55 , occurs where the intensities of the two Airy patterns are equal. Zero visibility occurs where there is a null in one of the Airy patterns. $|\mu_{12}|$, determined from the maximum value of the visibility, is equal to 0.8 and 0.55, respectively.

These results indicate a very high degree of spatial coherence throughout practically the entire laser beam. Figure 4 shows the experimental data together with a Gaussian profile $|\mu_{12}|$ curve with a coherence radius $R_c = 550 \mu\text{m}$. Considering the small size of the laser beam, we have observed a spatial coherent area containing almost half of the entire laser power, corresponding to a coherent power of more than 1 mW. This extraordinarily high degree of spatial coherence, combined with the high average power and narrow linewidth, makes this laser a powerful coherent photon source for applications. A stricter convention, sometimes used to define coherent area, allows $|\mu_{12}|$ to drop only to a value of 0.88 ($\sim e^{-1/8}$) [10]. Use of this stricter criteria would reduce the coherence radius to $\sim R_c/2$. Even so, about $\frac{1}{8}$ of the total power, or ~ 0.4 mW, is spatially coherent. Moreover, since this high coherent power is generated in only four pulses per second, with a pulsewidth of 1.5 ns each, the laser’s peak coherent power is estimated to reach 6×10^4 W. Assuming focusing with $f/10$ optics, this peak coherent power would produce a diffraction-limited focal spot with intensity reaching $2 \times 10^{13} \text{ W cm}^{-2}$. A coherent source should also be temporally coherent. This laser has a spectral bandwidth of $\Delta\lambda/\lambda \leq 1 \times 10^{-4}$, corresponding to a longitudinal coherence length longer than $300 \mu\text{m}$, sufficient for most applications. Therefore, it can be regarded as temporally coherent.

An additional parameter useful for characterizing a light source, and closely related to spatial coherence, is spectral brightness. Previous experiments on beam divergence have shown that this laser can be well approximated as originated from a virtual source located ~ 5 cm inside the capillary. We can estimate the size of this source using the van Cittert-Zernike theorem. To produce the same Gaussian coherence profile with $R_c = 550 \mu\text{m}$, the source should have a diameter (root mean square) of $d_s = \lambda z / \pi R_c = 5.4 \mu\text{m}$. With a measured divergence angle of 7 mrad (2θ) [27], the brightness of this source is then $\sim 1.6 \times 10^{17}$, in units of photons $\text{s}^{-1} \text{ mm}^{-2} \text{ mrad}^{-2}$ within 0.01% spectral bandwidth.

The peak brightness of this laser reaches a value of 2×10^{25} , making it one of the brightest soft-x-ray sources, all the more remarkable in that it is entirely contained on a single optical bench. No other soft-x-ray source, independent of its size, is presently capable of simultaneously generating such high average coherent power and peak spectral brightness.

In summary, we have observed an extraordinarily high degree of spatial coherence in high average power soft-x-ray laser beams produced by a tabletop device. The results were

obtained by single-pass laser amplification in a very long capillary plasma column using intrinsic mode-selection mechanisms. The availability of full spatial coherence in tabletop soft-x-ray laser beams with high average power and extremely high spectral brightness opens new opportunities in science and technology.

We gratefully acknowledge the support from the National Science Foundation, the Department of Energy, and Air Force Office of Scientific Research.

-
- [1] D. T. Attwood, *Soft X-rays and Extreme Ultraviolet Radiation* (Cambridge University Press, New York, 1999).
 - [2] J. J. Rocca, *Rev. Sci. Instrum.* **70**, 3799 (1999).
 - [3] Ch. Spielmann *et al.*, *Science* **278**, 661 (1997).
 - [4] A. Rundquist *et al.*, *Science* **280**, 1412 (1998).
 - [5] J. E. Trebes *et al.*, *Phys. Rev. Lett.* **68**, 588 (1992).
 - [6] Y. Kato *et al.*, in *Ultrashort Wavelength Lasers*, edited by S. Suckewer (SPIE, Bellingham, 1992), pp. 56–64.
 - [7] M. C. Marconi *et al.*, *Phys. Rev. Lett.* **79**, 2799 (1997).
 - [8] R. E. Burge *et al.*, *J. Opt. Soc. Am. B* **14**, 2742 (1997); **15**, 1620 (1998); **15**, 2515 (1998).
 - [9] More papers can be found in *X-Ray Lasers 1996*, edited by S. Svanberg and C-G. Wahlström (Institute of Physics, Bristol, 1996); *X-Ray Lasers 1998*, edited by Y. Kato, H. Takuma, and H. Daido (Institute of Physics, Bristol, 1998).
 - [10] M. Born and E. Wolf, *Principles of Optics*, 7th ed. (Cambridge University Press, Cambridge, 1999).
 - [11] D. T. Attwood, in *Proceedings of the First Symposium on the Applications of Laboratory X-Ray Lasers*, edited by N. M. Ceglio (Lawrence Livermore National Laboratory, Livermore, CA, 1985), CONF-850293-Abstracts, pp. 74–83.
 - [12] M. D. Rosen, J. E. Trebes, and D. L. Matthews, *Comments Plasma Phys. Control. Fusion* **10**, 245 (1987).
 - [13] R. A. London, *Phys. Fluids* **31**, 184 (1988).
 - [14] R. A. London, M. Strauss, and M. D. Rosen, *Phys. Rev. Lett.* **65**, 563 (1990).
 - [15] P. D. Gasparyan, F. A. Starikov, and A. N. Starostin, *Usp. Fiz. Nauk* **168**, 843 (1998) [*Phys. Usp.* **41**, 761 (1998)].
 - [16] P. Amendt, M. Strauss, and R. A. London, *Phys. Rev. A* **53**, R23 (1996).
 - [17] J. J. Rocca *et al.*, *Phys. Rev. Lett.* **73**, 2192 (1994).
 - [18] J. J. Rocca *et al.*, *Phys. Rev. Lett.* **77**, 1476 (1996).
 - [19] B. R. Benware *et al.*, *Phys. Rev. Lett.* **81**, 5804 (1998).
 - [20] C. D. Macchietto, B. R. Benware, and J. J. Rocca, *Opt. Lett.* **24**, 1115 (1999).
 - [21] J. W. Goodman, *Statistical Optics* (Wiley, New York, 1985), pp. 171–187.
 - [22] B. J. Thompson and E. Wolf, *J. Opt. Soc. Am.* **47**, 895 (1957).
 - [23] C. Chang *et al.*, *Opt. Commun.* **182**, 25 (2000).
 - [24] P. Lu *et al.*, *Phys. Rev. A* **58**, 628 (1998).
 - [25] T. Ditmire *et al.*, *Phys. Rev. Lett.* **77**, 4756 (1996).
 - [26] In this paper, we use coherence radius R_c to characterize the transverse coherence length. The definition of R_c is following the convention of coherence area A_c used in Ref. [21] as $\pi R_c^2 = A_c = \iint |\mu_{12}(\Delta x, \Delta y)|^2 d\Delta x d\Delta y$. Therefore, a Gaussian profile $|\mu_{12}|$ would be $|\mu_{12}(\Delta x, \Delta y)| = \exp[-(\Delta x^2 + \Delta y^2)/2R_c^2]$.
 - [27] As reported in Ref. [20], the peak-to-peak divergence angle is ~ 4.6 mrad; 7 mrad contains most of the laser energy.

Nanofabrication and diffractive optics for high-resolution x-ray applications

Erik H. Anderson,^{a)} Deirdre L. Olynick, Bruce Harteneck, Eugene Veklerov, Gregory Denbeaux, Weilin Chao, Angelic Lucero, Lewis Johnson, and David Attwood
E. O. Lawrence Berkeley National Laboratory, Mail Stop 2-400, 1 Cyclotron Road, Berkeley, California 94720

(Received 15 June 2000; accepted 5 September 2000)

Short wavelength x-ray radiation microscopy is well suited for a number of material and life science studies. The x-ray microscope (XM1) at the Advanced Light Source Synchrotron in Berkeley, California uses two diffractive Fresnel zone plate lenses. The first is a large condenser lens, which collects soft x-ray radiation from a bending magnet, focuses it, and serves as a linear monochromator. The second is the objective zone plate lens, which magnifies the image of the specimen onto a high-efficiency charge coupled device detector. The objective lens determines the numerical aperture and ultimate resolution. New objective lens zone plates with a minimum linewidth of 25 nm and excellent linewidth control have been fabricated using Berkeley Lab's 100 keV Nanowriter electron beam lithography tool, a calixarene high-resolution negative resist, and gold electroplating. Although the condenser zone plate is less critical to the resolution of the instrument, its efficiency determines the flux on the sample and ultimately the exposure time. A new condenser zone plate was fabricated and has a 9 mm diameter, 44 000 zones, and a minimum zone width of 54 nm (optimally the condenser and objective should have the same zone width). It is also fabricated with the Nanowriter at 100 keV using poly(methylmethacrylate) resist and nickel electroplating. The phase shift through the nickel absorber material enhances the diffraction efficiency over an amplitude only zone plate. To evaluate the microscope's performance transmission test patterns have been made and imaged. Lineout data show modulation for 30 nm lines and 60 (1:2) spaces to be almost 100%. These new diffractive optical elements represent a significant advancement in the field of high-resolution soft x-ray microscopy. Diffractive optical elements have been used to measure the wave front error of an extreme ultraviolet projection optical system. The reference wave is generated by the spherical wave generated by diffraction from a small freestanding pinhole. © 2000 American Vacuum Society. [S0734-211X(00)11106-0]

I. INTRODUCTION

In the soft x-ray region of the electromagnetic spectrum, materials suitable for fabricating refractive lenses are not available. Reflective focusing optics can be constructed using multilayer structures of different materials in limited wavelength regions as, for example, is used in extreme ultraviolet (EUV) lithography.¹ Large angle (grazing) incidence reflection can also be used to make focusing x-ray optics.² Optical elements based on diffraction, such as Fresnel zone plates, have shown very high resolution and are used in x-ray microscopes for probe formation and imaging. Instruments in which the x-ray beam is focused to a small spot and the sample or beam is scanned can provide a wealth of signals suitable for detection, transmitted x-ray intensity,³ photoelectron⁴ intensity and spectra, and fluorescence imaging.⁵ In addition to probe formation, zone plates are used as imaging elements to magnify the radiation transmitted through an object onto a suitable detector in a conventional microscope configuration. The XM1 microscope at Berkeley Laboratory's Advanced Light Source Synchrotron is configured as a conventional x-ray microscope.⁶

The position of the zones for a Fresnel zone plate are given by the equation

$$R^2(m) = m\lambda f + (m\lambda)^2/4,$$

where R is the radius of the zone, m an integer is the zone number, λ is the wavelength, and f is the focal length. Provided that the zone plate has enough zones (about 100) the outer zones act like a localized grating with period 2δ , where δ is the finest zone width. The numerical aperture of a zone plate is then $\lambda/(2\delta)$ and this sets the scale for the resolution of the lens. Therefore, the requirement for high spatial resolution forces the fabrication of the smallest zone width possible. High-resolution electron beam lithography is well suited for exposing the fine feature zones and other diffractive optics structures with the necessary pattern placement accuracy.

II. NANOWRITER HIGH RESOLUTION ELECTRON BEAM LITHOGRAPHY SYSTEM

Figure 1 shows a photograph of the lithography tool used for the fabrication of x-ray zone plates and other diffractive optical elements. This tool has the same electron optical column, stage, and support electronics of the Leica Microsystems VB6-HR⁷ system coupled with a unique digital pattern generator (DPG), ideally suited for curved structures, and control software developed internally at Berkeley Laboratory.⁸ The Leica column consists of a thermal field emission source for high brightness giving small probe size

^{a)}Electronic mail: EHAnderson@lbl.gov

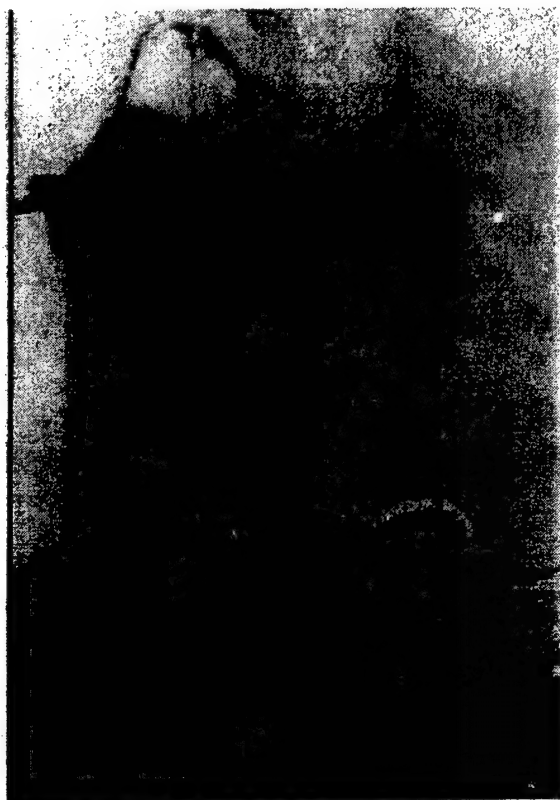


FIG. 1. Nanowriter electron beam lithography tool for ultrahigh resolution research and development lithography. Column, stage, and ancillaries built by Leica Microsystems. Digital Pattern Generator, data path, and control software developed at Lawrence Berkeley National Laboratory.

and high current. The accelerating voltage is variable between 20 and 100 kV with the best lithography results obtained at 100 kV. The stage has travel over approximately 150 mm by 150 mm area and incorporates a three axis (x , y , θ), $\lambda/1024$ (0.6 nm) resolution interferometer for positional measurement, feedback, and control. The vacuum system uses oil-free dry turbo and backing pumps for clean contamination-free operation. The sample holders are initially pumped in a load-lock and are transported by a robotic arm either directly to the stage or to one of two holding areas for temperature conditioning. Holders made by Leica are front surface referenced for height control and allow 3, 4, 5, 6, and 8 in. wafers as well as 6 in. square by 1/4 and 1/8 in. thick mask plates to be used. A transmitted electron detector is mounted directly under the stage for on-axis alignment and calibration.

The DPG delivers X and Y analog deflection signals for both the major (slow-speed and large deflection) and minor (high-speed and small deflection) amplifiers. The minor field size is 1/64 of the major field size and the amplifier has a 25 MHz bandwidth. The fine focus, X and Y stigmation signals are dynamically corrected by the DPG and fed into the respective correction coil amplifiers. The blanking signal from the DPG drives the high-speed blanking plate amplifier using differential ECL signals. The critical DPG electronics is

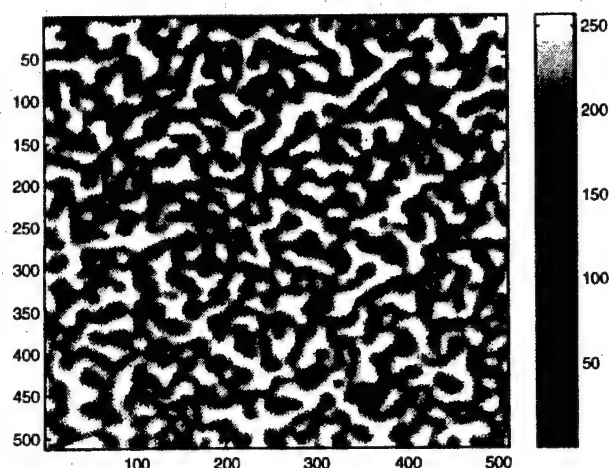


FIG. 2. Transmitted electron signal measured by the diode detector under the sample stage of gold "islands" used for alignment and calibration. The gold islands are formed by annealing 10 nm of evaporated gold for 60 min in a 170 °C oven on a 100 nm thick window of Si_3N_4 . These structures have high-spatial resolution and a sharp autocorrelation function. The x and y units are 2 nm/pixels.

physically located near the column to minimize signal path lengths and degradation. The control computer "talks" to the Leica subsystems such as the electron optics, stage, and robot control using a 10 Mbit/s ethernet interface. The control computer has a frame grabber board and high-speed image coprocessor board to rapidly evaluate numerically intensive fast Fourier transform calculations for correlation based mark detection.

A window wafer made of a 100 nm Si_3N_4 membrane with gold "islands" (10 nm evaporated gold annealed in air 60 min at 170 °C), is shown in Fig. 2, and is used to establish proper on-axis alignment. Using an automatic focus/stigmation algorithm that minimizes the size and nonroundness of the autocorrelation function, an array (typically 6 by 6) of data points is measured within the exposure field. The coefficients of a two dimensional polynomial function are determined by a singular value decomposition⁹ of the measured data values. The corrections are applied and repeated if necessary. In the larger fields, nonlinear distortion corrections become important. The laser feedback control of the stage is next calibrated by first taking an image of a reference mark and then moving the stage a short distance within the feedback range. A new image is taken and the process is repeated for four different positions of the stage. Cross-correlation functions are used to determine the positional change between the initial mark position and four subsequent measured positions. Again singular value decomposition is used to determine the proper feedback linear terms from the overdetermined set of data. When the laser feedback is properly calibrated the reference mark will appear to be stationary with the stage moving to different positions. After laser feedback calibration, the nonlinear distortions of the exposure field are measured and corrected in a similar way. First, an image of a reference mark is recorded in the center of the field. The stage and deflection are moved together in a two-

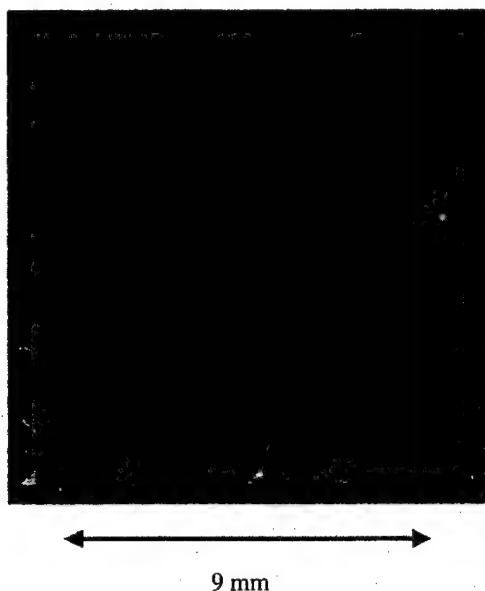


FIG. 3. Optical micrograph of the condenser zone plated fabricated using 100 keV electron beam lithography, PMMA resist, and nickel electroplating. The zone plate is 9 mm in diameter, has 41,000 zones, and a smallest zone width of 54 nm.

dimensional array throughout the field and subsequent images of the mark are taken at each point. The displacement at each point is determined by cross-correlation calculation between the reference image and mark image. Figure 3 shows the magnitude of the nonlinear corrections for a 524 μm exposure field and the final correction values. Accurate beam placement is critical for diffractive optics since placement errors introduce phase errors and the phase relationships across the entire optic surface must be a small fraction of the smallest linewidth. For diffraction limited resolution the phase error should be smaller than $\pi/8$ with a 25 nm outer zone width, the placement should be 25 nm/8 rms, giving 3σ placement of 9 nm or better. Finally, the minor field deflection is calibrated against the major field. A reference image is taken of a mark and compared with a set of four images taken with the minor field set to boundary limits and the major field set to an equal and opposite deflection. When properly aligned the reference mark remains stationary and deviations from the reference location are analyzed to apply corrections to the minor field scaling and rotation terms.

III. ZONEPLATE FABRICATION PROCESSING

A number of resist processes are used to take advantage of sensitivity and resolution tradeoffs. The resist with the highest resolution, "4-methyl-1-acetoxycalix[6]arene"^{10,11} also has the highest dose requirement. For the condenser zone plate, 950 molecular weight poly(methylmethacrylate) (PMMA) resist¹² was used. For other applications resists based on DUV chemically amplified products are used.¹³⁻¹⁵ The membrane windows for both the condenser and objective zone plates are formed by back etching a 100 nm thick Si_3N_4 coated wafer. The condenser window consists of four

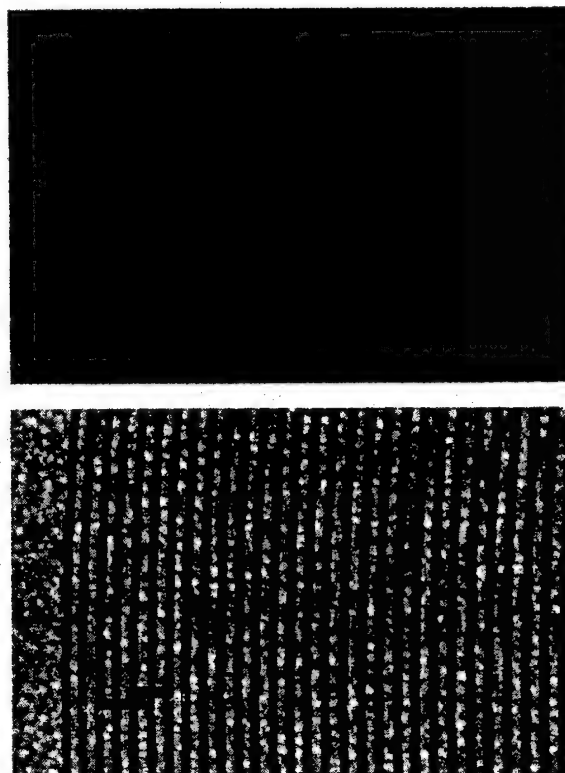


FIG. 4. SEM of an objective, microzoneplate. The outer zones, shown at the bottom are 25 nm and good linewidth control is observed across the structure.

5 mm square sections with "support" silicon structures. Larger windows, 10 mm by 10 mm, were first used but found to be easily broken during processing, and the area lost to the support structure was a small compromise necessary to achieve acceptable yield. Figure 4 shows the condenser zone plate and the support structure. A thin electroplating base of 5 nm chrome and 12 nm gold is evaporated onto the window wafer. A coating of PMMA is spun onto the wafer and baked at 170 $^{\circ}\text{C}$ for 90 min to form a thickness of 250 nm. The wafer is exposed with a 100 kV electron beam at a current of about 2.3 nA, slightly compromising ultimate system resolution but necessary to finish the exposure in a reasonable time, approximately 48 h. The wafer is developed in 2:1 ratio of isopropyl alcohol (IPA) and methyl-iso-butyl-ketone for 45 s, rinsed in IPA, and carefully dried with N_2 . The zone plate is then given a short plasma clean in oxygen to remove contamination from the plating base, typically removing 10 nm of PMMA. The wafer is electroplated in a commercial nickel plating solution¹⁶ with an apparatus developed to keep the solution clean and at a constant temperature. The plating progress is monitored by measurement of the difference in step height between the plated areas and the PMMA resist in an off zone plate test structure. After the plating is completed the PMMA is stripped in solvents and the wafer is cleaned.

The processing for the objective zone plate starts with a thin 100 μm thick window wafer (due to the mechanical requirements of the XM1 microscope) with 100 nm Si_3N_4

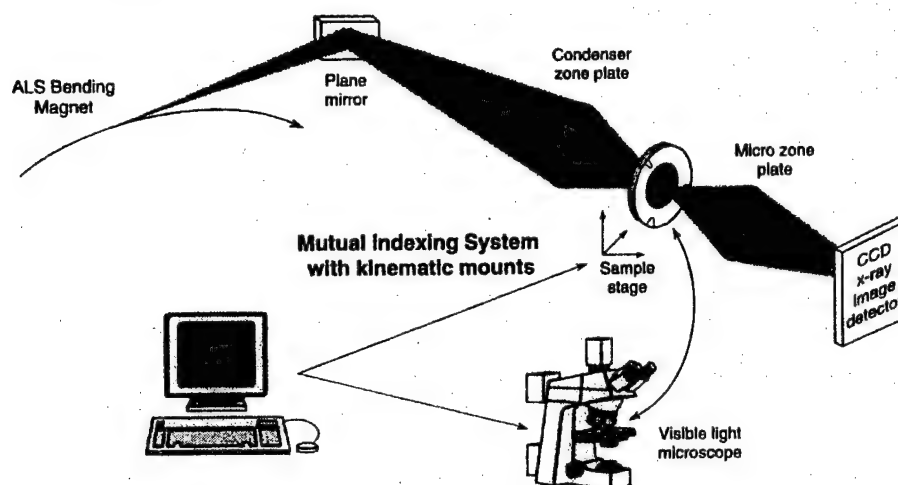


Fig. 5. Layout of XM1 x-ray microscope at the Advanced Light Source Synchrotron. The broad band radiation from a bending magnet is reflected off a nickel mirror at grazing incidence onto the condenser zone plate. This zone plate focuses the beam onto the sample. The condenser zone plate and the aperture at the sample plane form a linear monochromator. The radiation transmitted through the sample is imaged with high magnification onto the back thinned CCD detector.

membrane. Previous work demonstrated that calixarene resist produced smaller linewidth zone plates than PMMA.¹⁰ The full chemical name of this resist is "4-methyl-1-acetoxycalix[6]arene" and was purchased from the chemical company TCI America.¹⁷ This material did not fully dissolve in the solvent *o*-dichlorobenzene but fortunately when a small amount of dichloromethane was added the material dissolved. The calixarene resist is spin coated after chrome-gold plating base is evaporated and baked in an oven at 170°C for 30 min. The wafer is exposed under high-resolution beam conditions at 100 kV, 0.5 nA beam current at a dose of about 27 000 $\mu\text{C}/\text{cm}^2$. These very high dose and high-resolution beam conditions result in relatively long exposures (10 min each zone plate). The basic stability of the tool is required to complete the exposure without significant drift or change during the exposure time. The exposed samples are developed in xylenes for 30 s and rinsed in IPA for 30 s. The wafer is oxygen cleaned and plated in a commercial gold solution.¹⁸ A scanning electron-microscope (SEM) micrograph showing the electroplated structure is shown in Fig. 4. The gold lines at the edge of the zone plate have a linewidth of 25 nm and good linewidth control is observed across the sample. This is necessary but not sufficient for diffraction limited operation since zone placement is critical. The condenser and objective zone plates are installed at the XM1 microscope and used to study a variety of scientific samples.

IV. X-RAY MICROSCOPY IMAGES FROM XM1

The layout of the XM1 microscope beam line is shown in Fig. 5. The radiation from the bending magnet is reflected off a nickel coated flat mirror to remove the higher energy x rays, and collected by the condenser zone plate. The condenser focuses the radiation onto the sample through a small aperture, the combination of which forms a linear monochromator. Wavelengths longer or shorter than the desired wavelength are focused behind and ahead of the aperture, respectively. The soft x rays transmitted through the sample are imaged by the objective zone plate onto a sensitive back-

thinned charge coupled device (CCD) detector equipped with low noise readout electronics. Figure 6 shows a x-ray micrograph of thin gold 30 nm wide lines and 60 nm space grating and corresponding intensity lineout. The modulation of the lineout is almost 100%. Figure 7 shows 18 nm lines and 54 nm spaces with a high modulation lineout. Research is ongoing to determine the ultimate resolution limit of the system, which is estimated to be in the 20 nm range.

V. DIFFRACTIVE OPTICS FOR PHASE SHIFTING POINT DIFFRACTION INTERFEROMETRY

The development of optical systems for EUV lithography requires an accurate measurement of the system's wave front. A phase shifting point diffraction interferometer (PDI) described by Goldberg *et al.*¹⁹ is used for these measurements. The wave front under test is passed unperturbed through an aperture and a spherical wave front is produced by a small pinhole. The interference between these two patterns is recorded on a CCD detector and analyzed by a computer to determine the wave front aberrations. The critical diffractive element is this mask which contains the aperture

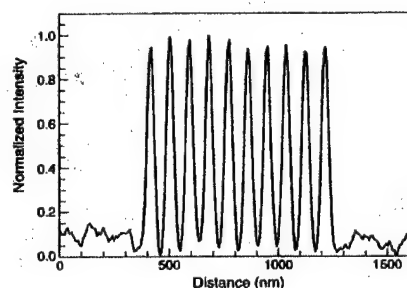


Fig. 6. X-ray micrograph of thin gold 30 nm lines and 90 nm period grating and corresponding intensity lineout. The modulation is almost 100%.

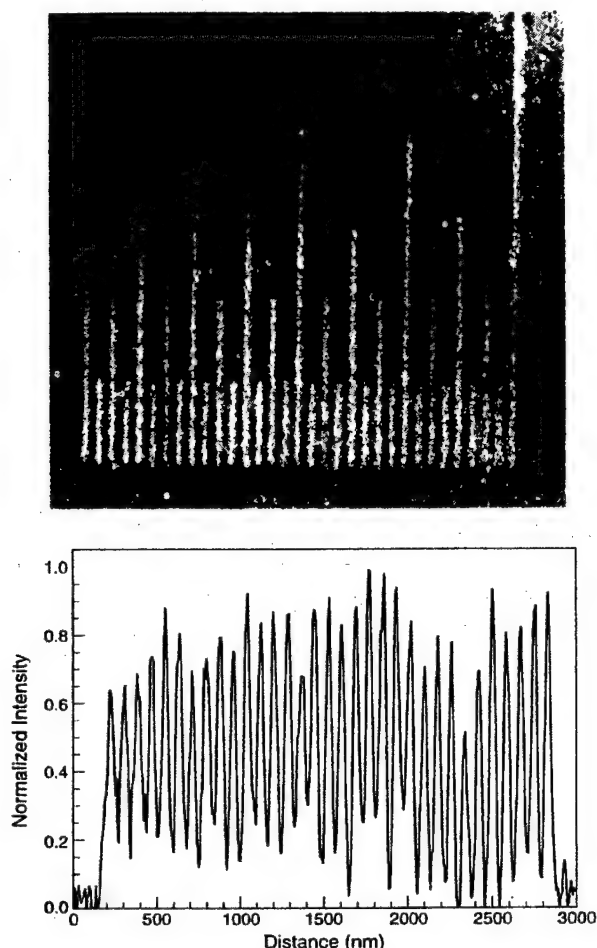


FIG. 7. X-ray micrograph of thin 18 nm lines and 72 nm period grating.

and pinhole, both of which must be “freestanding” to eliminate the introduction of artifacts from phase shifts in the membrane and the potential of beam induced contamination buildup. Figure 8 shows the PDI mask structure prior to etching. A wafer with Si_3N_4 windows is spin coated with a positive chemically amplified resist (KRS) invented by IBM.¹³ The wafers are soft baked on a hot plate for 2 min at 110 °C and the aperture and pinhole patterns are exposed with 100 kV lithography and developed using diluted MF312 developer. A postexposure bake is not required. The pattern is transferred by reactive ion etching of the Si_3N_4 all the way through the membrane. Care must be exercised to avoid overetching which will cause window breaking. After etching the absorber material, nickel is evaporated on both the front side and back side of the wafer. About 240 nm of nickel (total) can be evaporated before the added stress breaks the windows.

VI. CONCLUSION

Diffractive optical elements for x-ray applications stress the limits of nanofabrication due to the demanding requirements for fine linewidth structures and accurate image place-

80 - 120 nm Pinholes

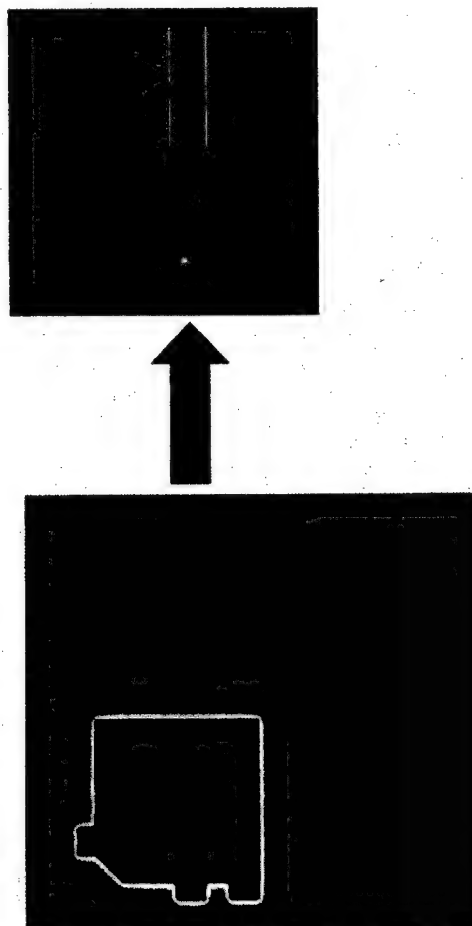


FIG. 8. SEM micrograph of phase shift point diffraction interferometer object structure used to pass the primary beam unaltered and generate a spherical reference beam. The interference pattern between the primary beam and the reference beam is recorded on a CCD imager and processed to provide information about the primary beam wave front.

ment. A high-resolution electron beam lithography tool, which incorporates unique pattern generation hardware, has been used to fabricate large condenser zone plates and 25 nm outer zone width objective zone plates. These Fresnel lenses have been installed at the XM1 x-ray microscope and used for a number of projects in life science and material science research. A free standing diffractive structure for a common-path phase shifting point diffraction interferometer was fabricated and used to make high-accuracy measurements of a large four mirror EUV optical system. The electron beam lithography tool has proven its capability to pattern fine linewidth structures with excellent pattern placement.

ACKNOWLEDGMENTS

This work was supported by the Defense Advanced Research Project Agency Advanced Lithography Program through the U.S. Department of Energy under Contract No. DE-AC03-76SF00098. The authors gratefully acknowledge

the contributions of Volker Boegli and Lawrence Muray in the electron beam lithography tool development, the late Werner Meyer-Ilse for x-ray microscopy with zone plate optics, Ken Goldberg and Patrick Naulleau for PID mask development, and Linda Geniesse for artwork preparation.

¹D. Tichenor *et al.*, *Proc. SPIE* **3997**, 48 (2000).

²P. Kirkpatrick and A. V. Baez, *J. Opt. Soc. Am.* **38**, 766 (1948).

³C. Jacobsen, S. Williams, E. Anderson, M. T. Browne, C. J. Buckley, D. Kern, J. Kirz, M. Rivers, and X. Zhang, *Opt. Commun.* **86**, 351 (1992).

⁴H. Ade, Ph.D. thesis, Physics Department, SUNY, Stony Brook, 1990.

⁵C. Jacobsen, S. Lindaas, S. Williams, and X. Zhang, *J. Microsc.* **172**, 121 (1993).

⁶W. Meyer-Ilse, T. Warwick, and D. Attwood, *X-Ray Microscopy* (AIP, New York, 1999), p. 129.

⁷B. H. Koek, T. Chisholm, A. J. V. Run, J. Romijn, and J. P. Davey, *Microelectron. Eng.* **23**, 81 (1994).

⁸E. H. Anderson, V. Boegli, and L. P. Muray, *J. Vac. Sci. Technol. B* **13**, 2529 (1995).

⁹W. H. Press, B. P. Flannery, S. A. Teukolsky, and W. T. Vetterling,

Numerical Recipes (Cambridge University Press, Cambridge, UK, 1986), p. 52.

¹⁰J. Fujita, Y. Ohnishi, Y. Ochiai, and S. Matsui, *Appl. Phys. Lett.* **68**, 1297 (1996).

¹¹S. Spector, C. Jacobsen, and D. Tennant, *J. Vac. Sci. Technol. B* **15**, 2872 (1997).

¹²Microlithography Chemical Company, 294 Pleasant St., Watertown, MA 02172.

¹³K. Y. Lee and W. S. Huang, *J. Vac. Sci. Technol. B* **11**, 2807 (1993).

¹⁴Z. Cui, A. Gerardino, M. Gentili, E. DiFabrizio, and P. D. Prewett, *J. Vac. Sci. Technol. B* **16**, 3284 (1998).

¹⁵E. A. Dobisz and C. R. K. Marrian, *J. Vac. Sci. Technol. B* **15**, 2327 (1997).

¹⁶Sulfamex make up solution, Enthone Omi, 350 Frontage Rd., West Haven, CT 06516.

¹⁷TCI America, 9211 North Harbortgate St., Portland, OR 97203.

¹⁸BDT510 make up solution, Enthone Omi, 350 Frontage Rd., West Haven, CT 06516.

¹⁹K. A. Goldberg, P. Naulleau, P. Batson, P. Denham, E. H. Anderson, H. Chapman, and J. Bokor, *J. Vac. Sci. Technol. B*, these proceedings.

PROCEEDINGS OF SPIE REPRINT



SPIE—The International Society for Optical Engineering

Reprinted from

Soft X-Ray and EUV Imaging Systems

**3–4 August 2000
San Diego, USA**



Volume 4146

©2000 by the Society of Photo-Optical Instrumentation Engineers
Box 10, Bellingham, Washington 98227 USA. Telephone 360/676-3290.

High Resolution Soft X-ray Microscopy

Weilun Chao^{1,2*}, Erik H. Anderson¹, Gregory Denbeaux¹, Bruce Harteneck¹, Mark Le Gros¹, Angelic L. Pearson¹, Deirdre Olynick¹, David Attwood^{1,2}

¹ Lawrence Berkeley National Laboratory, Berkeley, CA 94720

² University of California at Berkeley, Berkeley, CA 94720

ABSTRACT

The XM-1 is a soft x-ray full-field microscope that uses zone plates for the condenser and objective lenses. One of the main features of XM-1 is the high spatial resolution, which is made possible by the fine features of the objective zone plate. At present, the microscope uses a zone plate with an outer zone width of 25 nm. Several test patterns containing periodic lines and spaces were fabricated to measure the resolution of the microscope. Experimental data shows that the microscope can resolve 25 nm features. As simulations indicate that good contrast can be observed with even smaller features, test patterns with finer features are being fabricated to actually determine the resolution limit of the microscope.

Keywords: x-ray microscope, XM-1, zone plate, resolution

1. INTRODUCTION

The x-ray microscope is an extension of a visible light microscope to the x-ray region. It makes use of the differential absorption of the sample for imaging. The microscope not only provides very high resolution, but also a unique capability to image a thick sample in aqueous environment, which other kinds of high resolution microscopes (like electron microscopes or atomic force microscopes) do not have. X-ray interaction with matter allows the microscope to provide elemental and chemical contrast. All these unique features make this microscope very useful in biology, material science, and other areas^{1,2}.

At the Advanced Light Source (ALS) of Lawrence Berkeley National Laboratory (LBNL), we have a soft x-ray microscope XM-1 that operates between 250 eV and 900 eV. Our research is to measure the resolution of the system and understand the factors that affect it. In this paper, we will present the latest result of the resolution measurement.

2. SOFT X-RAY MICROSCOPE XM-1

In the full-field soft x-ray microscope XM-1, a plane mirror is illuminated by bending magnet radiation from the ALS (figure 1). The mirror reflects the radiation onto a condenser zone plate (CZP), which in turn focuses the light on the sample plane through a pinhole. The radiation from the sample is then imaged on the CCD by a micro zone plate (MZP). All the focusing is chosen to be performed by diffractive optics because in soft x-ray region the δ of the refraction index for most materials ($n = 1 - \delta + i\beta$) is much less than unity; conventional lenses would have to be very thick to produce the required amount of bending and would absorb most of the radiation.

The combination of the CZP and the pinhole serves as a monochromator to select a particular wavelength for imaging. Selection of the pinhole size is not trivial because of the trade-off between spectral resolution and radiation flux. A set of parameters (figure 1) with pinhole size of 15 μm was chosen to give $\lambda/\Delta\lambda \sim 700$ ³, which is sufficient for our applications.

Both zone plates were fabricated in the Nanofabrication Laboratory in the Center for X-ray Optics (CXRO)⁴. As resolution depends on the outer zone width of a zone plate, our goal is to fabricate micro zone plates with the outer zones as small as

* Correspondence: Email: wchao@lbl.gov; Telephone: 510-486-4079; Fax: 510-486-4550.

possible. Currently, using the Nanowriter, we are able to obtain zone plates with 25-nm outer zone width (figure 2). The parameters of the MZP are listed in figure 1.

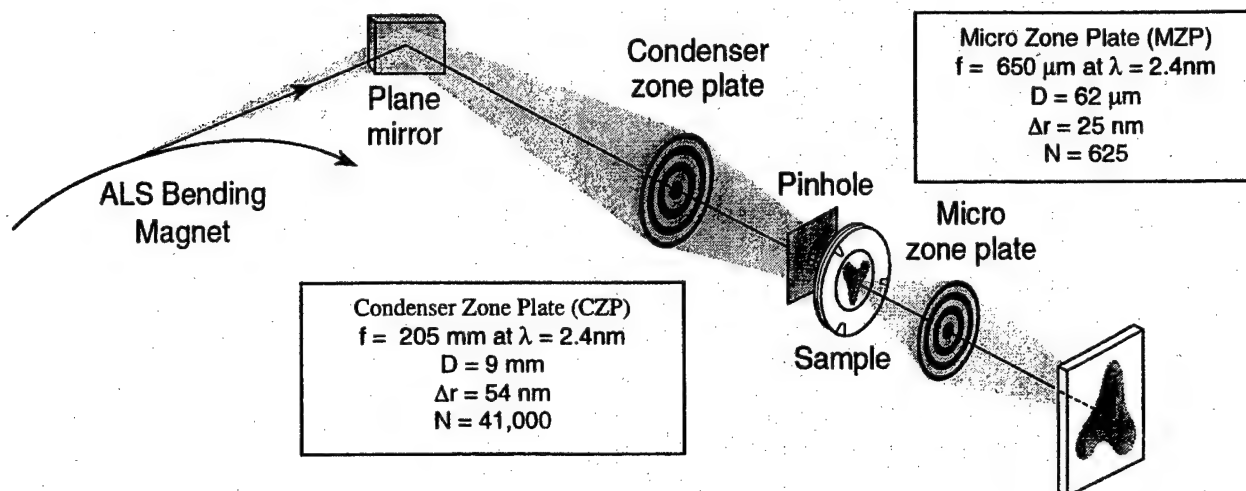


Figure 1. Schematics of the Soft X-ray Microscope XM-1 at beamline 6.1.2 of the Advanced Light Source (ALS). Bending magnet radiation from the ALS is used to illuminate the sample. The degree of partial coherence of the system is 0.45

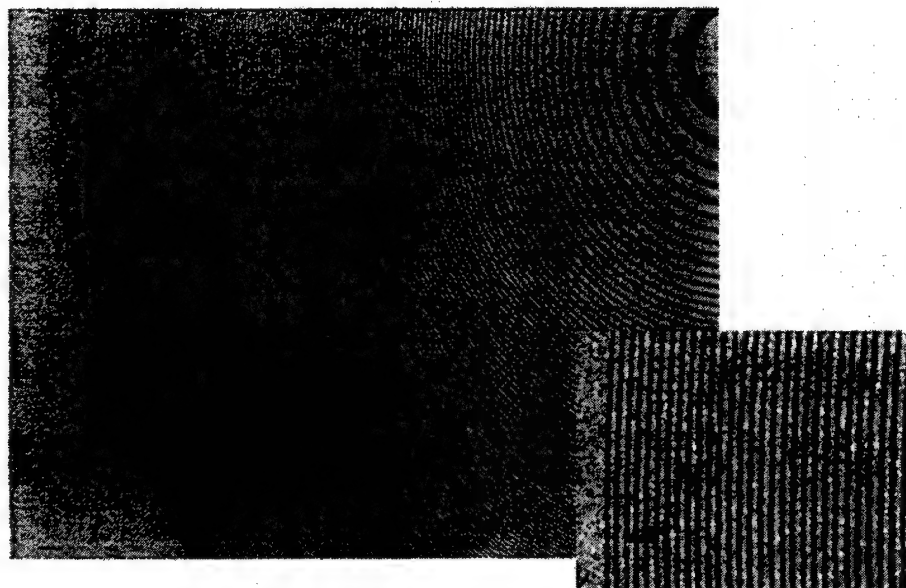


Figure 2. An SEM micrograph of the current 25 nm micro zone plate (MZP). Both the condenser and the micro zone plates are fabricated with the Nanowriter electron beam lithography tool in the Nanofabrication Laboratory. The resolution of the microscope is determined in large part by the outer zone width of the MZP.

3. TEST PATTERNS

Several test objects have been made for measuring the resolution of the system. They consist of lines and spaces with different periods and duty cycles. One of them is shown in figure 3. They were fabricated by the same lithography tool as used for the zone plates. To determine the resolution limit of the system, test patterns with feature sizes as small as the

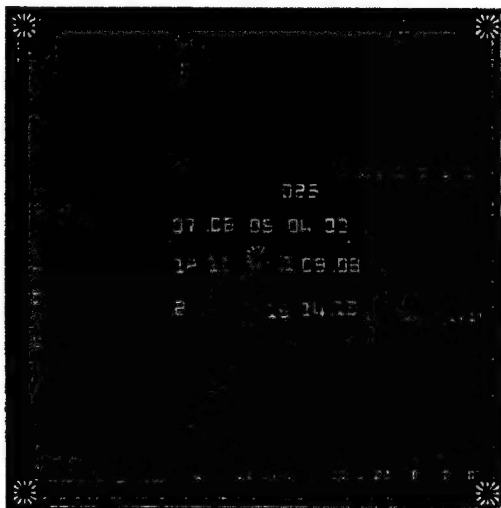


Figure 3. One of the test objects used for resolution measurement. This gold-plated object contains two sets of lines and spaces with linewidths from 30 nm to 250 nm. One set has line-to-space ratio of 1:1, another has the ratio of 1:2. The center of the object has a set of elbows with linewidths as narrow as 25 nm. The dimension of this test object is 120 μm X 120 μm

resolution are needed. The resolution of the microscope is expected to be slightly below the outer zone width of the MZP, depending on the partial coherence of the system. However, the current outer zone width is close to the limit of the fabrication tool. Thus, determination of resolution is not straightforward. Several resists, including Calixarene and HSO, and different fabrication techniques have been experimented for obtaining high quality lines and spaces with small periods⁴. The latest test object, which is one of our best, was made with HSO resist and was plated with nominally 40-nm thick gold. Resist between the lines was not etched away to maintain the quality of the patterns.

4. RESULTS

Our latest test object has recently been imaged under the microscope. Figure 4 shows images of some of the lines and spaces with small periods, along with their corresponding SEM images. Because of the lack of "landmarks" on the object, the x-ray images and SEM images might not be taken from the same location. The x-ray images were taken at wavelength of 2.4 nm with 3100x magnification. The x-ray images have pixel sizes of 8 nm.

The x-ray images clearly shows that the patterns can be resolved by the microscope. The normalized lineout of the 15 nm lines and 35 nm spaces gives us a measured contrast of 24%. Figure 5 shows the experimental contrast as a function of the spatial frequency of the corresponding patterns. The theoretical cutoff of the microscope, which depends on the numerical apertures of the KZP and MZP, is about 17 nm half-period. Along with the assumption that large features would have 100% contrast, the points are fitted with a numerical curve. Lines and spaces with a half-period of 23 nm are predicted to yield 15.3% contrast, which is the Rayleigh criterion.

5. FUTURE WORK

Currently, the Nanofabrication laboratory is upgrading its etching system. The new system will enhance our capability to fabricate test patterns of higher quality with feature size smaller than the expected resolution. To understand the factors that affect the resolution, we will also develop a theoretical model and compare the experimental contrasts with the prediction.

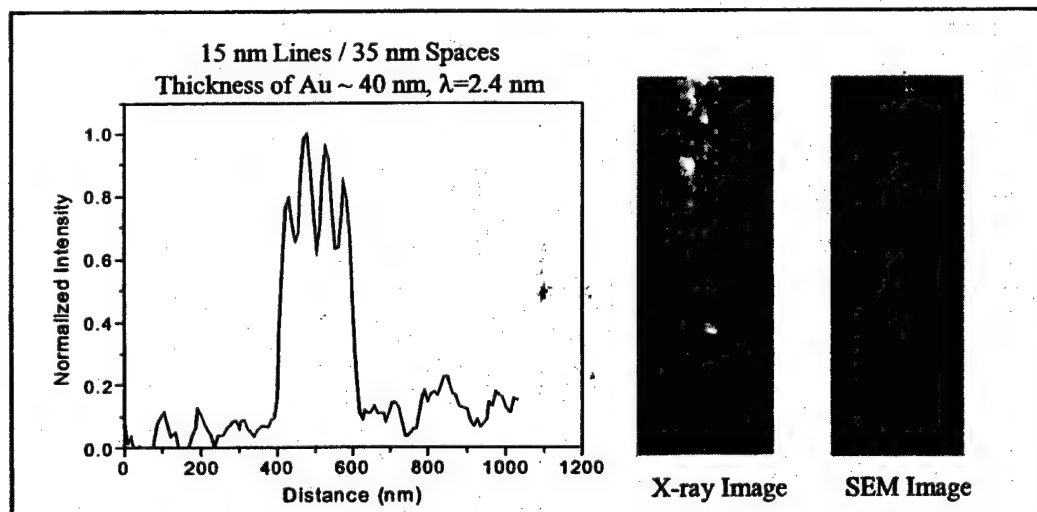
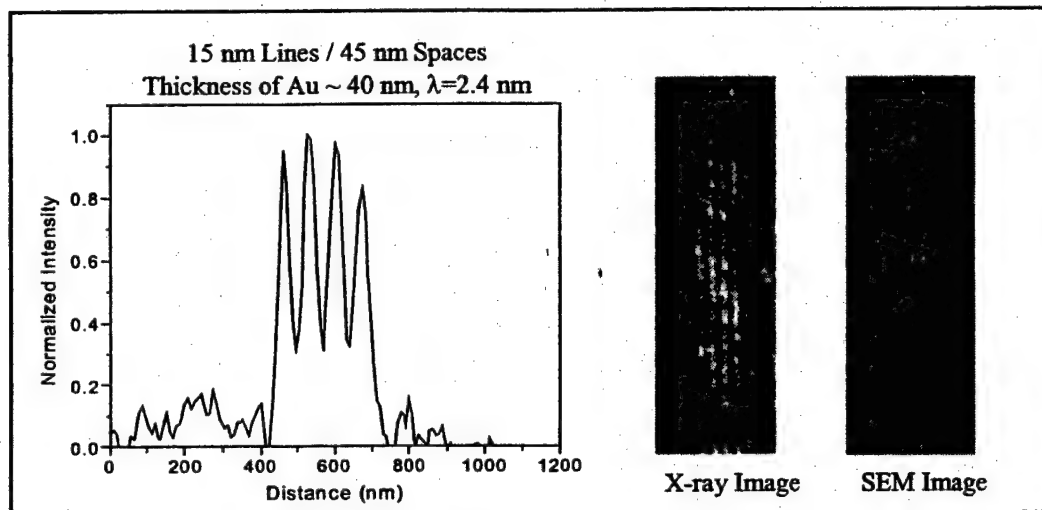
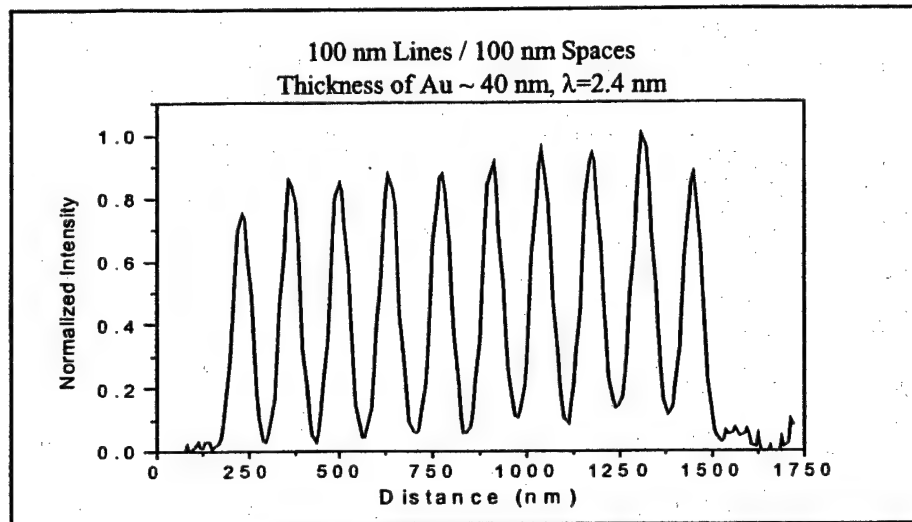


Figure 4. X-ray and SEM images of lines and spaces with different periods. The SEM and X-ray images may not be taken at the same location. Both have the pixel size of 8 nm. The normalized lineout of 15 nm lines and 35 nm spaces has 24% contrast.

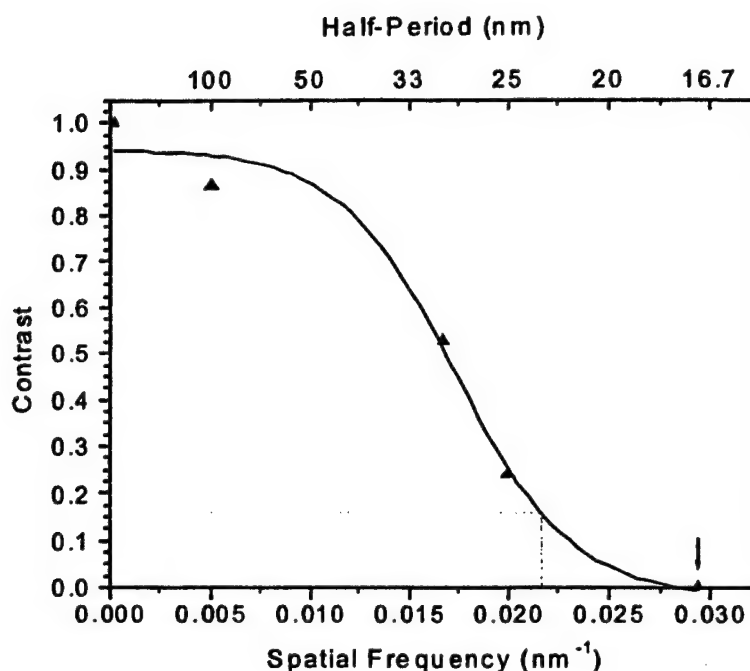


Figure 5. Experimental contrast of different periods. Also shown is the calculated cutoff (half-period of 17 nm) of the microscope. The solid line is a least squares fit to the experimental data, the cutoff, and an assumed value of unity at zero spatial frequency. The Rayleigh criterion of 15.3% contrast corresponds to a half-period of 23 nm.

ACKNOWLEDGEMENTS

The authors would like to thank the Department of Energy's Office of Basic Energy Sciences, DARPA, and the Air Force Office of Scientific Research for their generous support.

REFERENCES

1. W. Meyer-Ilse, G. Denbeaux, L. Johnson, W. Bates, A. Lucero, and E. H. Anderson, "The High Resolution X-ray Microscope, XM-1," *X-Ray Microscopy*, Edited by W. Meyer-Ilse, T. Warwick and D. Attwood, AIP, New York, 1999, pp. 129-134.
2. A. L. Pearson, W. Chao, G. Denbeaux, T. Eimuller, P. Fischer, L. Johnson, M. Koehler, C. Larabell, M. Le Gros, D. Yager, and D. Attwood, "XM-1, the high-resolution soft x-ray microscope at the Advanced Light Source," *Soft X-Ray and EUV Imaging Systems*, Edited by W. M. Kaiser and R. H. Stulen, SPIE 4146, (2000).
3. G. Denbeaux, L.E. Johnson, and W. Meyer-Ilse, "Spectroscopy at the XM-1," *X-Ray Microscopy*, Edited by W. Meyer-Ilse, T. Warwick and D. Attwood, AIP, New York, 1999, pp. 478-483.
4. E. H. Anderson, D. L. Olynick, B. Harteneck, E. Veklerov, G. Denbeaux, W. Chao, A. Lucero, L. Johnson, and D. Attwood Jr., "Nanofabrication and Diffractive Optics For High-Resolution X-Ray Applications," *J. Vac. Sci Techn.*, (2000), to be published.

PROCEEDINGS OF SPIE REPRINT



SPIE—The International Society for Optical Engineering

Reprinted from

X-Ray Micro- and Nano-Focusing: Applications and Techniques II

**30 July 2001
San Diego, USA**



Volume 4499

©2001 by the Society of Photo-Optical Instrumentation Engineers
P.O. Box 10, Bellingham, Washington 98227 USA. Telephone 360/676-3290.

Experimental Analysis of High-Resolution Soft X-ray Microscopy

Weilun Chao^{1,2**}, Erik H. Anderson¹, Gregory Denbeaux¹, Bruce Harteneck¹, Angelic L. Pearson¹,
Deirdre Olynick¹, Gerd Schneider¹, David Attwood^{1,2}

¹ Center for X-ray Optics, Lawrence Berkeley National Laboratory, CA 94720

² University of California at Berkeley, CA 94720

ABSTRACT

The soft x-ray, full-field microscope XM-1 at Lawrence Berkeley National Laboratory's (LBNL) Advanced Light Source has already demonstrated its capability to resolve 25-nm features. This was accomplished using a micro zone plate (MZIP) with an outer zone width of 25 nm. Limited by the aspect ratio of the resist used in the fabrication, the gold-plating thickness of that zone plate is around 40 nm. However, some applications, in particular, biological imaging, prefer improved efficiency, which can be achieved by high-aspect-ratio zone plates. We accomplish this by using a bilayer-resist process in the zone plate fabrication. As our first attempt, a 40-nm-outer-zone-width MZIP with a nickel-plating thickness of 150 nm (aspect ratio of 4:1) was successfully fabricated. Relative to the 25-nm MZIP, this zone plate is ten times more efficient. Using this high-efficiency MZIP, a line test pattern with half period of 30 nm is resolved by the microscope at photon energy of 500 eV. Furthermore, with a new multilayer mirror, the XM-1 can now perform imaging up to 1.8 keV. An image of a line test pattern with half period of 40 nm has a measured modulation of 90%. The image was taken at 1.77 keV with the high-efficiency MZIP with an outer zone width of 35 nm and a nickel-plating thickness of 180 nm (aspect ratio of 5:1). XM-1 provides a gateway to high-resolution imaging at high energy. To measure frequency response of the XM-1, a partially annealed gold "island" pattern was chosen as a test object. After comparison with the SEM image of the pattern, the microscope has the measured cutoff of 19 nm, close to the theoretical one of 17 nm. The normalized frequency response, which is the ratio of the power density of the soft x-ray image to that of the SEM image, is shown in this paper.

Keywords: soft x-ray microscope, XM-1, high aspect ratio, zone plate, resolution, gold island pattern.

1. INTRODUCTION

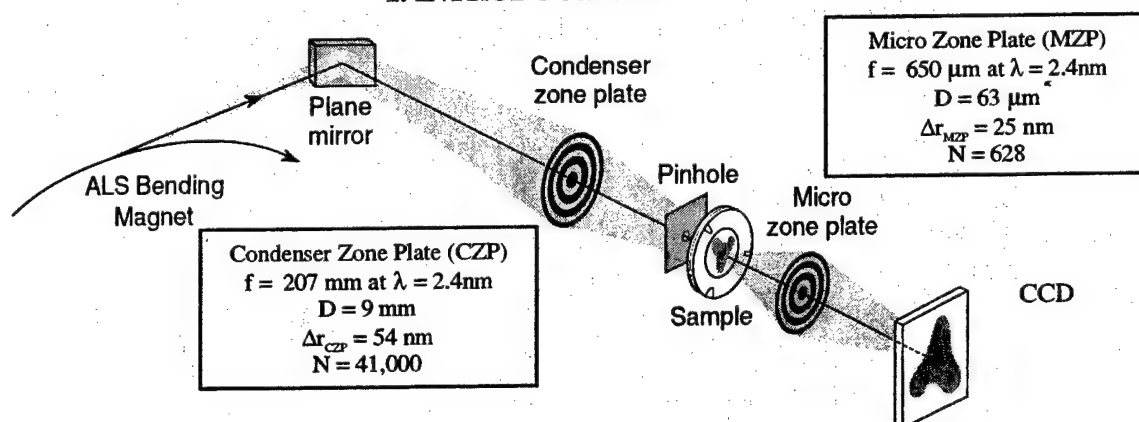


Figure 1. The layout of the soft x-ray microscope XM-1 at beamline 6.1.2 of the Advanced Light Source (ALS). Bending magnet radiation from the ALS is used to illuminate the sample, which is in air. The combination of numerical apertures of the two zone plates produces partially coherent imaging condition, with σ equal to $\Delta r_{MZIP} / \Delta r_{CZP} = 0.45$

* Correspondence: wlchao@lbl.gov ; Phone: 510-486-4079; Fax: 510-486-4550; Lawrence Berkeley National Laboratory, 1 Cyclotron Road, MS 2-400, Berkeley, CA 94720.

The soft x-ray microscope XM-1 at LBNL's Advanced Light Source (ALS) synchrotron radiation facility is an extension of a visible light microscope to the soft x-ray region^{1,2}. It uses radiation from a bending magnet in the ALS to illuminate its sample, which is in air. Because XM-1 is operated in the soft x-ray region (from 300 eV to 1.8 keV), it can be used to image wet samples up to 10 μm thick in the full-field transmission mode, which is an advantage over other high-resolution microscopes like TEM.

Figure 1 shows the layout of XM-1. Bending magnet radiation from the ALS is reflected by a plane mirror onto a condenser zone plate (CZP), which in turn focuses the radiation on the sample through a pinhole. The radiation passing through the sample is then imaged onto a charge-coupled device (CCD) using a micro zone plate (MZP). Both the CZP and MZP are fabricated in the Nanofabrication Laboratory in the Center for X-ray Optics (CXRO)³. The spatial resolution of the microscope is determined in part by the outer zone width of the MZP. Currently, the highest-resolution MZPs have an outer zone width of 25 nm (figure 2). With this zone plate, XM-1 has demonstrated its capability to resolve 25-nm-half-period features⁴.

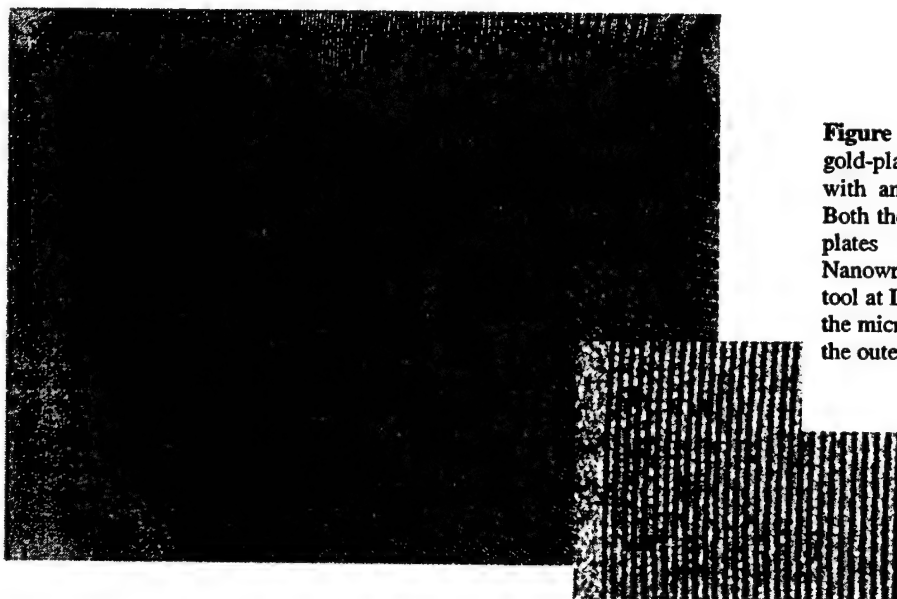
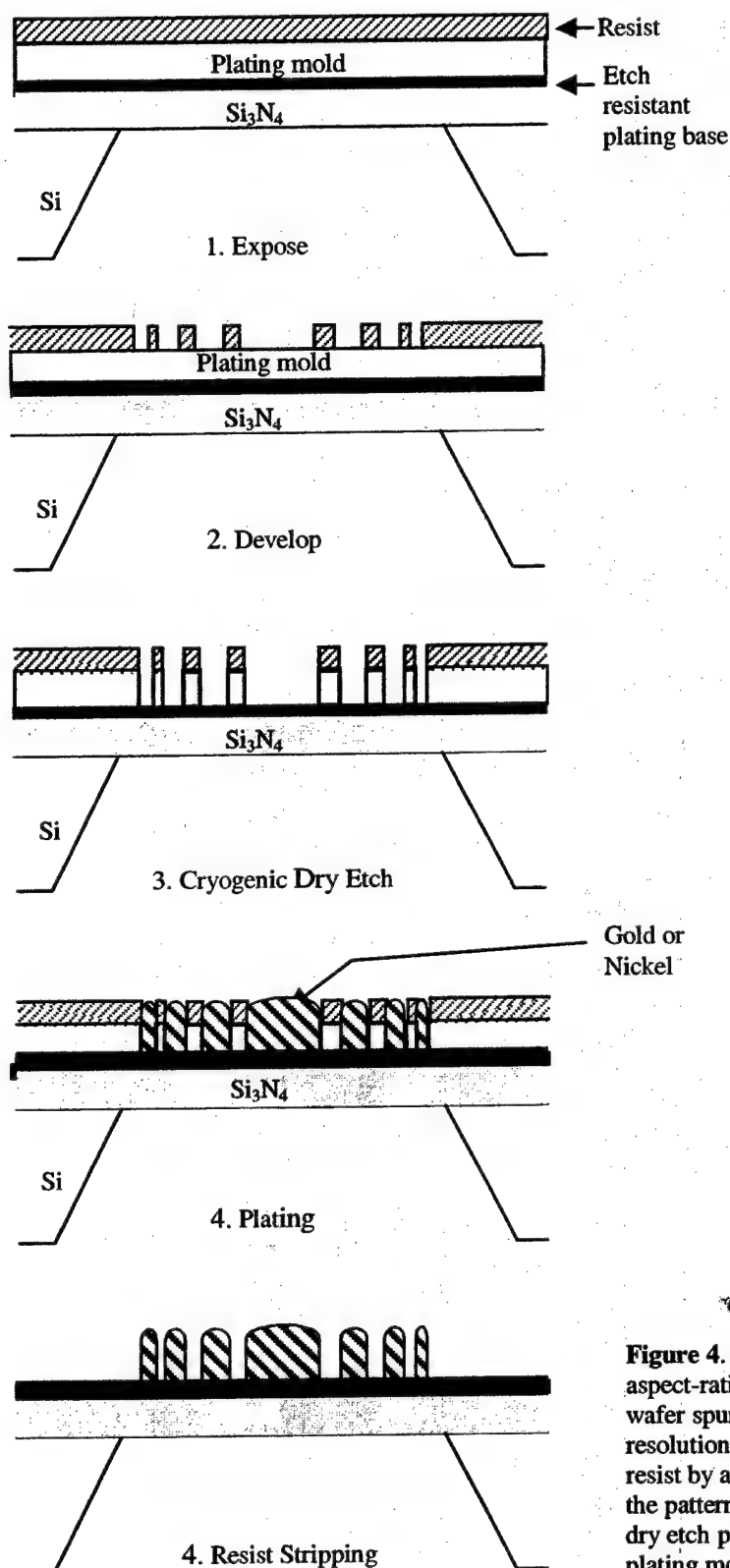


Figure 2. A SEM micrograph of the gold-plated micro zone plate (MZP) with an outer zone width of 25 nm. Both the condenser and the micro zone plates are fabricated with the Nanowriter electron beam lithography tool at LNBL. The spatial resolution of the microscope is determined in part by the outer zone width of the MZP.



Figure 3. One of the test objects used for resolution measurement. This 120 μm X 120 μm test pattern plated with 40-nm-thick gold contains two sets of line patterns with linewidths from 30 nm to 250 nm. One set has line-to-space ratio of 1:1, the other has a ratio of 1:2. The center of the object has a set of elbow patterns with linewidths as narrow as 25 nm. This object is used in most of the measurements in this paper.



In addition to very high spatial resolution, the microscope also has a good energy spectral resolution, which is determined by the geometry of the CZP and the pinhole. The current spectral resolution $\lambda/\Delta\lambda$ with a stationary condenser illumination is around 700 over a $9\text{-}\mu\text{m}^2$ field⁵, which allows users to perform elemental-sensitive imaging including magnetic material imaging⁶.

To characterize the spatial resolution of XM-1, several test objects with line patterns of different periods and duty cycles were fabricated using the same lithography tool as used for the zone plates. One of them, which is used in most of the measurements in this paper, is shown in figure 3. It was fabricated using the Nanowriter electron beam tool to write the pattern into Calixarene resist, followed by gold plating. The plating thickness of is nominally 40 nm.

2. HIGH-EFFICIENCY MICRO ZONE PLATE

The 25-nm-outer-zone-width MZP provides very high resolution. However, due to the current limitations in fabricating such a fine structure, the gold-plated MZP is relatively thin (about 40 nm). For some of our applications (in particular, biological imaging), where radiation dose is required to be minimal, improved efficiency of the MZP is preferred. This requires a high-aspect-ratio MZP. We accomplish this by the development of a bilayer-resist process.

In the bilayer-resist process, a high-resolution-resist layer and a layer of plating mold, a material that forms a mold for plating, are used for pattern formation (figure 4). The resist acts as a recording layer, where the pattern is written using a high-resolution electron beam. The

Figure 4. The bilayer-resist process is used to fabricate high-aspect-ratio zone plates. First, a Si-supported membrane wafer spun with a layer of plating mold and a layer of high-resolution resist is prepared. A pattern is then written into the resist by a high-resolution electron beam. After development, the pattern is transferred to the plating mold using a cryogenic dry etch process. The wafer is then plated. The resist and the plating mold are then stripped to obtain the final patterned object,

pattern is then transferred into the plating mold using a cryogenic dry etch process. This etch process is chosen because the use of the cold temperature (cryogenic) and gaseous etch chemicals (dry etching) reduces the vertical-sidewall etching. The patterned wafer is then plated with gold or nickel.

The bilayer-resist process allows fabrication of fine structures with relative high aspect ratio. In our case, HydrogenSilsesQuioxane (HSQ) and hardbaked AZPN114 are used as the resist and plating mold, respectively. The HSQ layer is about 40 nm thick and the structure is plated with either gold or nickel after the dry etching of the plating mold.

In our first attempt we began by fabricating 40-nm-outer-zone-width MZPs for better yield. The nickel-plating thickness of the zone plate is around 150 nm (aspect ratio of 4:1). Using one of these MZPs, the line patterns in the test object in figure 3 were imaged at the wavelength of 2.4 nm. The images of patterns with half periods of 30 nm and 40 nm and their corresponding lineouts are shown in figure 5. Both the 30-nm and 40-nm patterns are resolved by the microscope, with a corresponding modulation of 28% and 43%. Relative to the 25-nm-outer-zone-width MZP, this zone plate is 10 times more efficient.

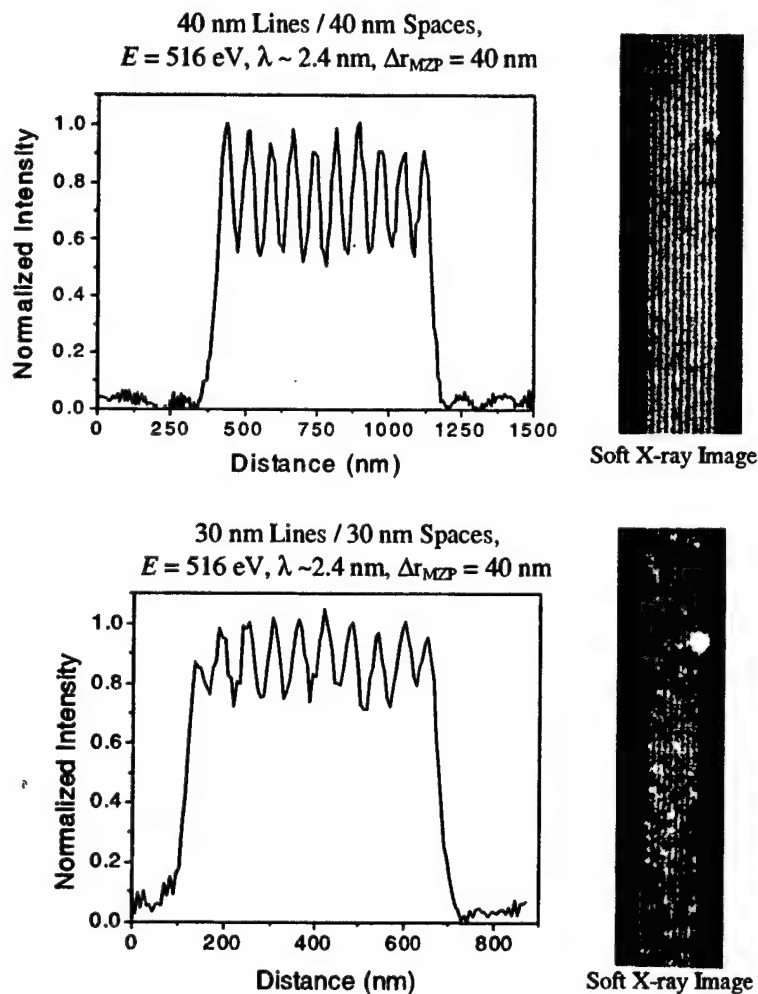


Figure 5. The line patterns with half periods of 30 nm and 40 nm were imaged with the 150-nm-thick, high-efficiency nickel MZP with the smallest zone width of 40 nm. Both 30-nm and 40-nm patterns are clearly resolved by the microscope, with the modulation of 28% in the 30-nm case.

Recently, 35-nm-outer-zone-width MZPs with a nickel-plating thickness of 180 nm (aspect ratio of 5:1) have been fabricated. They have been used in high-energy imaging experiments discussed in the following section.

3. HIGH-ENERGY IMAGING

As shown in figure 1, a plane mirror reflects bending magnet radiation to the microscope. The purpose of this mirror is to cut off high-energy photons. The nickel mirror used previously had a reflectivity of less than 15% for photon energies higher than the Ni L_3 edge, near 850 eV⁷. Motivated by interconnect⁸ and magnetic material imaging (e.g., Ni and Gd), we upgraded the nickel mirror to a multilayer mirror⁹. This enables XM-1 to perform imaging with energies up to 1.8 keV. Figure 6 shows the accumulation of 5 images of a line pattern with a half period of 40 nm. It was taken with a 35-nm-outer-zone-width MZP with a thickness of 180 nm (aspect ratio of 5:1) at 1.77 keV ($\lambda \sim 0.7$ nm).

At this photon energy, the 40-nm-thick gold plating of the line pattern absorbs only about 10 % of the incoming light, as compared to 60% at the photon energy of 500 eV. Based on the relationship between a pattern's natural contrast (C) and the number of photons needed to be collected in the pattern's image (N) to obtain a given signal-to-noise ratio (SNR), i.e. $N \propto 1/C^2$, an image at the energy of 1.8 keV would require 61 times more photons than that imaged at 500 eV to acquire the same SNR. Furthermore, for a given number of incoming photons, the CCD camera converts 1.8 keV/500 eV ~ 4 times more electron-hole pairs at the energy of 1.8 keV than at 500 eV (for simplicity, the photon-energy dependence of the quantum efficiency is ignored). Thus, to have the same image fidelity, an image taken at 1.8-keV energy needs about 240 times more counts than that at 500-eV energy. All of our images taken at different photon energies have similar number of counts. Therefore, the SNR of an accumulation of 5 images at 1.77-keV energy is $240/5 \sim 50$ times worse than that of a single image taken at 500-eV energy. This difference is shown clearly when the images in figure 5 and 6 are compared with each other.

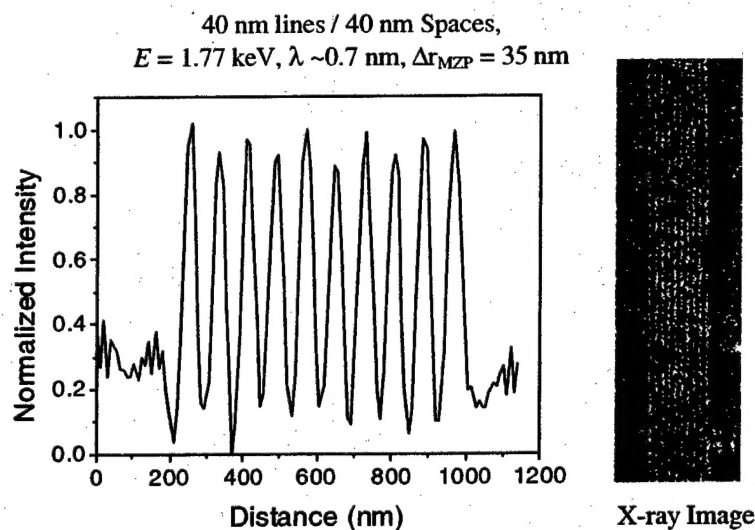


Figure 6. Shown are the accumulation of 5 images (after contrast and brightness adjustment) and the corresponding lineout of a line pattern with a half period of 40 nm taken at the energy of 1.77 keV. The MZP used in the imaging has the outer zone width of 35 nm and a nickel-plating thickness of 180 nm. The lineout shows a large modulation (90%) after averaging over the entire length of the image and normalized.

To obtain a low-noise lineout, the accumulated image is averaged along its length. Because of low absorption of the gold plating, the line-pattern's contrast in the CCD image is low. Normalization is needed to make the lineout more discernible. The normalized lineout is plotted in figure 6 and shows a surprisingly good modulation of 90%. Because the data analysis is sensitive to the high background and noise statistics, a further investigation of the modulation is in progress.

4. GOLD "ISLAND" SPECTRAL ANALYSIS

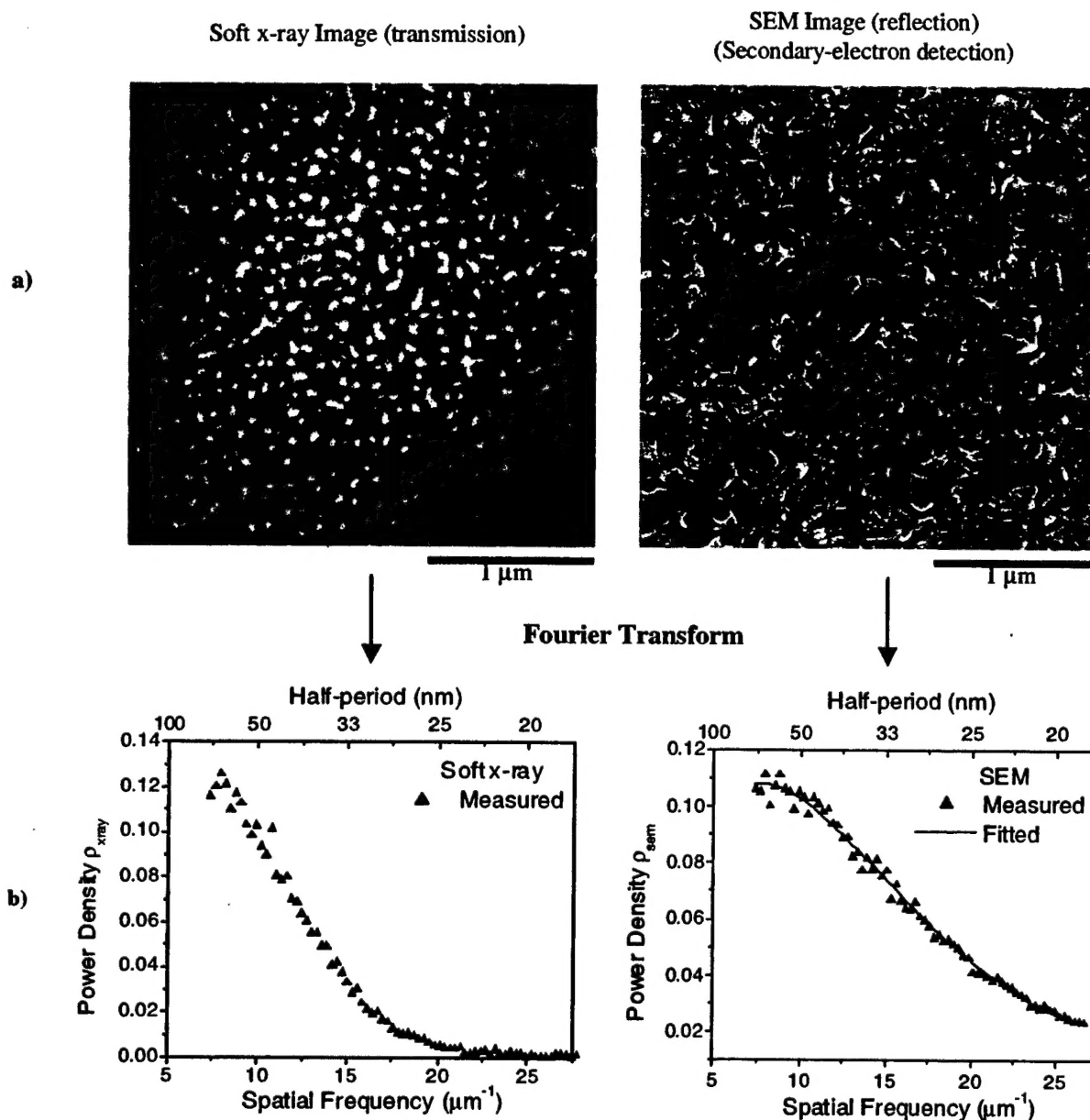


Figure 7. The gold "island" pattern was chosen for measurement of the frequency response of XM-1. a) The soft x-ray and SEM images of the gold pattern. The images were not taken at the same location. The pixel size for both images is 8 nm and the x-ray image was obtained with the 25-nm MZP at the wavelength of 2.4 nm. b) The power densities of the corresponding images. The density of the SEM image is fitted with polynomials to eliminate fluctuations in the data.

One of the deficiencies of the line patterns is that the response of the microscope is measured only at a single spatial frequency. Many patterns with different periods are required to obtain the response over a wide range of frequency. Moreover, when the period is small, it is difficult to obtain a high-quality pattern. The imperfections in the pattern will complicate the analysis of the images.

To overcome these difficulties, we employed a pattern of gold "islands" with sizes randomly distributed. This sample is prepared by annealing a 10-nm-thick gold layer on a thin Si_3N_4 membrane for an hour at 170 °C. At this temperature, the gold will tend to aggregate and form "islands". Because a large and pseudo-continuous range of feature sizes (from a few nm to about 100 nm) is obtained without any complicated nanofabrication processes, this pattern is ideal for measurement of frequency response of the microscope.

Figure 7a shows the soft x-ray image and SEM micrograph of the gold island pattern. The x-ray image was taken at a wavelength of 2.4 nm with the 25-nm-outer-zone-width lens described in figure 2. The projected pixel sizes are 8 nm for both images. The images were taken at different locations. However, this does not affect our analysis, as the dimensional distribution of the islands is the same at different locations due to the randomness of the gold islands. To obtain the power spectrum of the images, the images are first Fourier transformed, then averaged along the circumferences of circles centered at the zero frequency component (figure 7b). The power spectrum of the SEM image is fitted with polynomials to eliminate fluctuations in the spectrum.

Assuming the power spectrum of the SEM image to be the true spectrum of the pattern, a normalized frequency response of XM-1 is obtained by dividing the power spectrum of the soft x-ray image by that of the SEM image (figure 8). The normalized response shows that XM-1 has a 10% response to 25-nm-half-period features, which is consistent with our resolution test pattern images. The response curve extends to a cutoff at 19-nm half-period. This compares favorably with a prediction of 17 nm, based on an ideal zone plates with an outer zone width of 25 nm and a partially coherent illumination with σ equal to 0.45.

One should note that however, because of the nature of the partial coherence imaging, the normalized response only approximates the true response of XM-1, which is given by its transmission cross coefficient.

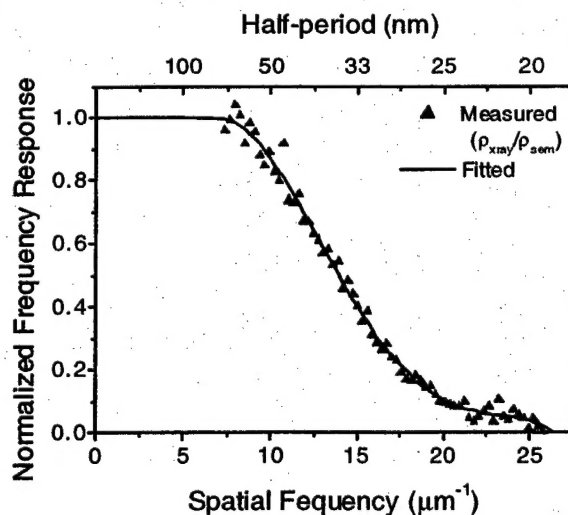


Figure 8. The normalized frequency response, obtained by dividing the power density of the soft x-ray image (ρ_{xray}) by that of the SEM image (ρ_{sem}), is plotted as a function of spatial frequency (bottom axis) and half period (top axis). 10% response is measured at a half period of 25 nm, which is consistent with our resolution measurements. The response cuts off around 19-nm half-period, which is slightly bigger than the theoretical cutoff of 17-nm half-period.

5. CONCLUSIONS

With the use of a bilayer-resist process, high-efficiency zone plates with an aspect ratio of 5:1 were fabricated successfully. These lenses improve diffraction efficiency, and thus greatly shorten the exposure time of our images. Along with a new beamline mirror, the MZPs enable the microscope to perform very-high-resolution imaging up to 2 keV energy range. Our next step is to extend our fabrication process to high-efficiency zone plates with finer zones.

ACKNOWLEDGEMENTS

This work was supported by the Director, Office of Science, Office of Basic Energy Sciences, of the U.S. Department of Energy, by DARPA, of the U.S. Department of Defense, and by the Air Force Office of Scientific Research.

REFERENCES

1. W. Meyer-Ilse, H. Medeck, L. Jochum, E. Anderson, D. Attwood, C. Magowan, R. Balhorn, M. Moronne, D. Rudolph, G. Schmahl, "New High-resolution Zone-plate Microscope at Beamline 6.1 of the ALS," *Synchrotron Radiation News*, **8**, pp. 22-23 (1995)
2. G. Denbeaux, E. Anderson, W. Chao, T. Eimüller, L. Johnson, M. Köhler, C. Larabell, M. Legros, P. Fischer, A. Pearson, G. Schütz, D. Yager and D. Attwood, "Soft X-ray microscopy to 25 nm with applications to biology and magnetic materials," *Nuclear Instruments and Methods in Physics Research Section Accelerators, Spectrometers, Detectors and Associated Equipment*, Volumes 467-468, Part 2, pp. 841-844 (2001)
3. E. H. Anderson, D. L. Olynick, B. Harteneck, E. Veklerov, G. Denbeaux, W. Chao, A. Lucero, L. Johnson, and D. Attwood Jr., "Nanofabrication and Diffractive Optics For High-Resolution X-Ray Applications," *J. Vac. Sci. Techn. B* **18**(6), 2970-2975 (2000)
4. W. Chao, E. H. Anderson, G. Denbeaux, B. Harteneck, M. Le Gros, A. L. Pearson, D. Olynick, D. Attwood, "High Resolution Soft X-ray Microscopy," *Soft X-Ray and EUV Imaging Systems*, Edited by W. M. Kaiser and R. H. Stulen, SPIE 4146, pp. 171-175 (2000)
5. G. Denbeaux, L. E. Johnson, and W. Meyer-Ilse, "Spectroscopy at the XM-1," *X-Ray Microscopy*, Edited by W. Meyer-Ilse, T. Warwick and D. Attwood, AIP, New York, 1999, pp. 478-483.
6. G. Denbeaux, P. Fischer, G. Kusinski, M. Le Gros, A. Pearson, and D. Attwood, "A Full Field Transmission X-ray Microscope as a tool for High-Resolution Magnetic Imaging," *IEEE Trans. on Magnetics*, **37**(4), pp. 2764-2766 (2001)
7. B. L. Henke, E. M. Gullikson and J. C. Davis, "X-Ray Interactions: Photoabsorption, Scattering, Transmission, and Reflection at $E = 50\text{-}30,000$ eV, $Z = 1\text{-}92$," *Atomic Data and Nucl. Data Tables*, **54**, 181 pp. 191-342 (1993). Current updates are maintained by E. M. Gullikson at http://www-cxro.lbl.gov/optical_constants/
8. G. Schneider, D. Hambach, B. Niemann, B. Kaulich, J. Susini, N. Hoffmann, and W. Hasse, "In situ x-ray microscopic observation of the electromigration in passivated Cu interconnects," *Appl. Phys. Lett.*, **74**, pp. 1936-1938 (2001)
9. G. Schneider, G. Denbeaux, F. Salmassi, and P. Nachimuthu, to be published.